JGR Space Physics

RESEARCH ARTICLE
10.1029/2022JA030356

Local Mapping of Polar Ionospheric Electrodynamics

K. M. Laundal[1], J. P. Reistad[1], S. M. Hatch[1], M. Madelaire[1], S. Walker[1], A. Ø. Hovland[1], A. Ohma[1], V. G. Merkin[2], and K. A. Sorathia[2]

[1]Department of Physics and Technology, Birkeland Centre for Space Science, University in Bergen, Bergen, Norway, [2]Applied Physics Laboratory, Johns Hopkins University, Laurel, MD, USA

Key Points:

- We present a technique to use disparate data types to produce local maps of polar ionospheric electrodynamics
- **ΔB** and convection measurements are related via ionospheric Ohm's law and spherical elementary current systems
- We demonstrate the technique on real and synthetic data, and discuss limitations and future development

Correspondence to:
K. M. Laundal,
karl.laundal@uib.no

Citation:
Laundal, K. M., Reistad, J. P., Hatch, S. M., Madelaire, M., Walker, S., Hovland, A. Ø., et al. (2022). Local mapping of polar ionospheric electrodynamics. *Journal of Geophysical Research: Space Physics*, *127*, e2022JA030356. https://doi.org/10.1029/2022JA030356

Received 4 FEB 2022
Accepted 15 APR 2022

Abstract An accurate description of the state of the ionosphere is crucial for understanding the physics of Earth's coupling to space, including many potentially hazardous space weather phenomena. To support this effort, ground networks of magnetometer stations, optical instruments, and radars have been deployed. However, the spatial coverage of such networks is naturally restricted by the distribution of land mass and access to necessary infrastructure. We present a new technique for local mapping of polar ionospheric electrodynamics, for use in regions with high data density, such as Fennoscandia and North America. The technique is based on spherical elementary current systems (SECS), which were originally developed to map ionospheric currents. We expand their use by linking magnetic field perturbations in space and on ground, convection measurements from space and ground, and conductance measurements, via the ionospheric Ohm's law. The result is a technique that is similar to the Assimilative Mapping of Ionospheric Electrodynamics (AMIE) technique, but tailored for regional analyses of arbitrary spatial extent and resolution. We demonstrate our technique on synthetic data, and with real data from three different regions. We also discuss limitations of the technique and potential areas for improvement.

Plain Language Summary The ionosphere, where a small but significant fraction of the atmosphere is ionized, forms the edge of space. At only 100-km altitude, it is the region in space which is by far best monitored by human instruments. Space scientists routinely use measurements that inform about specific aspects of the dynamics in the ionosphere, but not the whole picture. For example, magnetometers on ground measure one part of the electric current system while magnetometers on satellites measure another part. Radars measure the flow of charged particles in the ionosphere, while optical images and particle measurements can be used to estimate electric conductivity. In this paper, we present a technique that combines all these different types of measurements to give a complete picture of what takes place in the ionosphere. The technique is tailored for use in regions where the data density is high, and the spatial resolution and extent of the analysis region are flexible.

1. Introduction

Polar ionospheric electrodynamics can be thought of as a focused image of what takes place much further away from the Earth, in the magnetosphere. However, this is overly simplistic since the ionosphere also resists and reacts to this forcing via collisions with neutrals. The tug-of-war between magnetospheric driving and ion-neutral collisions leads to complex patterns of magnetic field disturbance and electric currents, whose relation to the imposed plasma flow may be counter-intuitive and difficult to untangle. Nevertheless, measurements are much more abundant near the ionosphere than higher up, and therefore offer an invaluable source of information for understanding the coupling between the Earth and the solar wind. Ground magnetometer measurements have been used to chart ionospheric currents for more than a century (Birkeland, 1901; Vestine et al., 1947), and space magnetometers have been used since the early space age (Iijima & Potemra, 1978); and both have provided fundamental knowledge about how the Earth and Sun are coupled. In the last decades, satellite (Heppner & Maynard, 1987) and radar (Ruohoniemi & Baker, 1998) measurements have given us maps of ionospheric convection that reveal the Sun-Earth coupling in even greater detail.

Several statistical studies and empirical models exist that describe how ionospheric convection (or electric fields; Förster & Haaland, 2015; Pettigrew et al., 2010; Weimer, 2005) and magnetic field perturbations (or currents; Edwards et al., 2020; Laundal et al., 2018; Weimer, 2013) vary as a function of seasons and solar wind conditions. These statistical models are useful for helping us understand the coupling between the solar wind and geospace in steady state, but they almost never capture the dynamics of this coupling. Maps based on global networks

of measurements offer a much better alternative for studies of ionospheric dynamics. For example, the SuperMAG network of magnetometers (Gjerloev, 2012) has been used to derive global maps of ground magnetic field perturbations at 1-min time resolution (Waters et al., 2015); the network of SuperDARN radars has been used to derive global maps of ionospheric convection, also at 1-min time resolution (Gjerloev et al., 2018; Ruohoniemi & Baker, 1998); and the fleet of Iridium satellites carry magnetometers that are used to derive global maps of field-aligned currents (FACs) with effectively 10-min time resolution (Anderson et al., 2000; Waters et al., 2020). To derive similar maps of ionospheric conductance at high time resolution, one can use global satellite images of the UV aurora (Frey et al., 2003), which were sporadically available between 1996 and 2005 when NASA's Polar and IMAGE satellite missions were active. Chains of ground-based observatories (GBOs; Mende et al., 2008) can also give valuable information about auroral conductance. Unfortunately, the availability of global maps of conductance, convection, FACs, and ground magnetic field perturbations do not all overlap in time.

Even with these global maps we only achieve partial views of ionospheric electrodynamics, one parameter at a time. Their utility can be increased through data assimilation, combining observations with theoretical models to obtain a more complete view of ionospheric electrodynamics. A pioneering step toward this end was made by Kamide et al. (1981), who presented what has become known as the "KRM technique." The KRM technique uses ground magnetic field measurements in combination with conductance maps to calculate the ionospheric convection and electric field. They calculated the curl of the ionospheric Ohm's law to derive a partial differential equation that relates ground magnetic field disturbances and the electric field. This approach is also at the foundation of the Assimilative Mapping of Ionospheric Electrodynamics (AMIE) technique introduced by Richmond and Kamide (1988). AMIE uses magnetic field measurements from ground and space, and ionospheric convection or electric field measurements in an inversion for the electric field. The electric field is represented with spherical cap harmonics (Haines, 1985), basis functions that cover the entire region poleward of some chosen latitude—typically 50°. AMIE also assumes that the ionospheric Ohm's law is valid (discussed further in Section 2.3), and it requires that the ionospheric Hall and Pedersen conductances are known or solved for in a separate inversion (Lu, 2017). The AMIE technique has been successfully used for more than three decades, and is still being actively developed to ingest the global data sets mentioned above, and to improve error estimates and stability (AMGeO Collaboration, 2019; Cousins et al., 2015; Matsuo, 2020).

AMIE yields patterns of ionospheric electrodynamics that cover the entire region poleward of 50°. However, the observations used in the inversion are never evenly distributed. This is illustrated in Figure 1, which shows data from SuperMAG, Iridium, and SuperDARN collected during a 4-min interval starting at 01:00 UT 5 April 2012. SuperMAG horizontal magnetic field perturbations are shown in orange. They are rotated 90° clockwise to align with an equivalent overhead current—a hypothetical horizontal sheet current in the ionosphere consistent with the observed magnetic field. Iridium horizontal magnetic field measurements, provided via the Active Magnetosphere and Planetary Electrodynamics Response Experiment (AMPERE; Anderson et al., 2017), are shown in blue. The green dots show the locations where the SuperDARN radars could estimate line-of-sight convection velocities during these minutes. We see that the data density is much higher in North America and in Fennoscandia compared to the rest of the polar region. AMIE inversions therefore have much stronger observational support in some regions of the map than others. The high data density in some regions could also support a better spatial resolution than can be justified in global analyses. This elicits the need for analysis techniques that are more flexible with respect to spatial scale and extent. In addition to the nonuniform data distribution on a global scale, there are certain measurements that can resolve very small-scale structures, which would also benefit from analysis techniques with high spatial resolution. Examples include convection and conductivity measurements in the field of view of phased array incoherent scatter radars, conductance distributions based on optical measurements from GBOs (Clayton et al., 2019; Grubbs et al., 2018), and high-resolution scans of the mesospheric magnetic field along the track of the upcoming Electrojet Zeeman Imaging Explorer (EZIE) satellites (Laundal et al., 2021; Yee et al., 2017).

Several alternatives to spherical harmonic analysis exist, which may be more suitable for regional analyses of ionospheric electrodynamics. Amm (1997) introduced spherical elementary current systems (SECS), basis functions that describe vector fields on a spherical shell that point either east-west or north-south relative to the pole at which they are placed. The former type is divergence-free, and the latter type is curl-free. The amplitude of the SECS functions falls off rapidly away from the pole, which makes them well suited for regional modeling. A

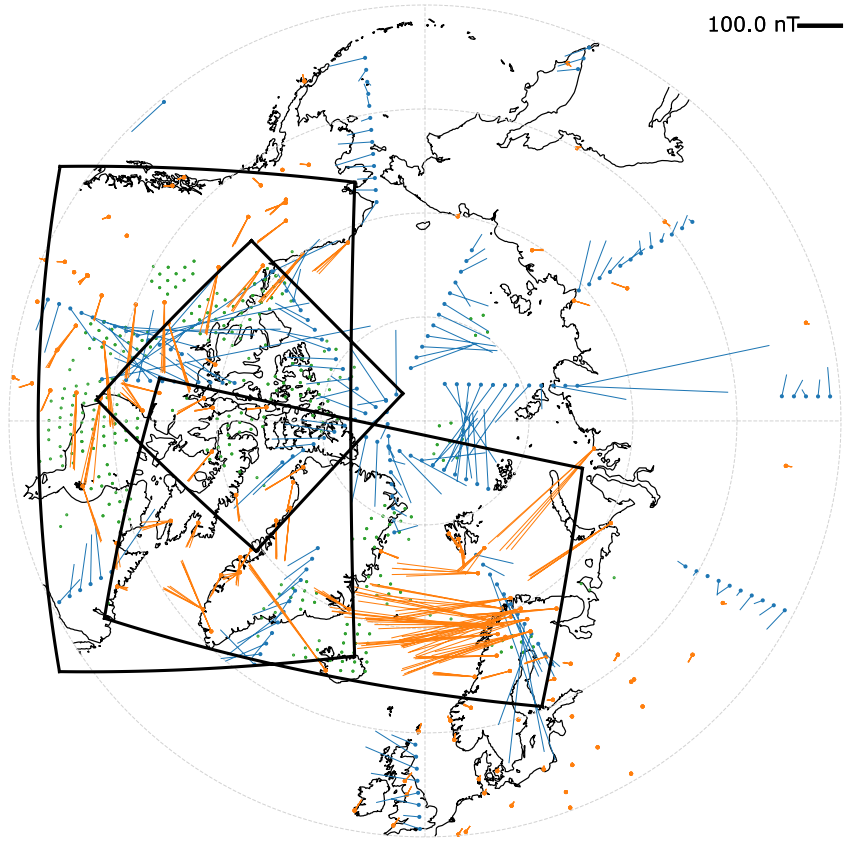

Figure 1. Example distribution of ionospheric electrodynamics measurements, from a 4-min period starting at 01:00 UT, 5 April 2012. The blue lines represent horizontal magnetic field disturbances measured from the fleet of Iridium satellites, provided by AMPERE. The orange lines represent horizontal magnetic field disturbances on ground, from SuperMAG. A scale for the Iridium and SuperMAG magnetic field vectors is shown in the top right corner. The green dots represent the locations of SuperDARN backscatter, which provides estimates of the line-of-sight plasma convection velocity. The frames show the extent of the grids used in example figures in Section 4.

superposition of SECS functions can represent any well-behaved vector field on a sphere, provided that they are placed sufficiently densely and scaled appropriately.

Historically SECS analysis has been used mostly for regional studies of equivalent currents (e.g., Amm, 1997; Amm & Viljanen, 1999; Amm et al., 2002; Laundal et al., 2021; Weygand et al., 2011). However, global studies are also possible (Juusola et al., 2014). SECS basis functions can also be used to represent ionospheric convection velocity (Amm et al., 2010) or electric fields (Reistad et al., 2019, 2019). SECS play an important part in the technique presented here, so we return to a detailed description of their definition and key properties below. We note that there are other options for representing electric fields or plasma flow in a regional grid: Nakano et al. (2020) presented an analysis technique for ionospheric plasma convection that uses basis functions similar to SECS, but without a singularity at the pole. Nicolls et al. (2014) used radar line-of-sight convection measurements to constrain a grid of electric potential values. The measurements and potential values were related via a matrix that numerically evaluates the gradient of the potential, i.e., the electric field components. Bristow et al. (2016), instead of fitting an electric potential (a curl-free vector function), fitted a divergence-free velocity to a set of SuperDARN radar measurements in a limited region with high data density.

The regional studies mentioned above were all concerned with one quantity at the time, and did not combine data as in the KRM or AMIE techniques. An SECS equivalent to the KRM technique, calculating the electric field from the equivalent current and ionospheric conductivity, was presented by Vanhamäki and Amm (2007), but it involves a multistep inversion technique which may be difficult to control.

In this paper, we present an SECS equivalent to the AMIE technique, of which KRM is a subset. Our technique has one single matrix that relates many different kinds of quantities at any location to a single set of model parameters. To find the model parameters, we can combine measurements of magnetic field perturbations on ground and in space, plasma convection, ionospheric electric field, or even FACs, in an inversion. When the model parameters are known, the same quantities can be calculated as output at any location within the analysis region. That means that if we know one quantity (e.g., the magnetic field on ground), and the ionospheric conductance, everything else can be calculated. The extent of the analysis region and the spatial resolution is flexible.

We call this method "Local mapping of polar ionospheric electrodynamics," or Lompe (not to be confused with the Norwegian potato-based flatbread). The theoretical basis for the Lompe technique, including how we use results from SECS analysis to relate electric and magnetic fields, is presented in Section 2. In Section 3, we describe in detail the numerical implementation of the technique. Example results from synthetic and real data sets are presented in Section 4. Some limitations and future prospects are discussed in Section 5, and Section 6 concludes the paper. Python code to reproduce the figures in this paper, and to use the Lompe technique for other events, is publicly available (Laundal et al., 2022).

2. Theoretical Background

In this section, we describe the theoretical background for the Lompe technique. We seek to relate four different quantities: Ionospheric electric fields, F-region plasma convection velocities, ground magnetic field disturbances, and space magnetic field disturbances. The purpose of this discussion is to precisely describe the assumptions that we make and the associated theoretical limitations. The numerical implementation, and associated limitations, are discussed in Section 3.

2.1. Electric Field

We choose to represent the ionospheric electric field as a sum of curl-free SECS (Amm, 1997; Vanhamäki & Juusola, 2020) in a grid on a spherical shell with radius R_I, the radius of our model ionosphere. Physically, this corresponds to modeling the electric field in terms of electric charge densities on a set of discrete lines that extend radially from R_I to infinity (Reistad et al., 2019). In this model, the electric field above R_I is horizontal, and it decreases as $1/r$ as the radial lines must be equipotentials. The use of curl-free local basis functions to represent $\mathbf{E}$ implies an assumption that, by Faraday's law, $\frac{\partial \mathbf{B}}{\partial t} = 0$.

Our task is to find the magnitudes of these vertical line charge densities that best fit the available measurements and prior knowledge. Mathematically, we express the electric field as

$$\mathbf{E} = \sum_i \frac{-m_i}{4\pi R_I} \cot\left(\frac{\pi/2 - \lambda_i}{2}\right) \hat{\mathbf{n}}_i, \tag{1}$$

where the sum is over a grid of SECS poles that will be discussed in detail in Section 3; λ_i is the latitude in a coordinate system where the ith SECS pole defines the north pole; $\hat{\mathbf{n}}_i$ is a unit vector that points northward in this local coordinate system; and m_i is the amplitude of the ith SECS pole. The product $m_i \epsilon_0$, where ϵ_0 is the vacuum permittivity, has a unit of line charge density C/m (Reistad et al., 2019). The negative sign in Equation 1 is included to make it consistent with the convention from earlier papers (e.g., Vanhamäki & Juusola, 2020), which refer to the $-\hat{\mathbf{n}}_i$ direction.

We stick to the historical designation of SECS, even though it is misleading in the context of electric fields. While most applications of SECS analysis have focused on electric currents, Amm et al. (2010) and Reistad et al. (2019) demonstrated its usefulness in analyses of ionospheric convection and associated electric field.

The electric field representation in Equation 1 is a starting point of the Lompe technique. In the following, we will describe how we relate the electric field to F-region ion velocity and magnetic field disturbances on ground and in space, and in Section 3, we specify how we relate all quantities to the set of SECS amplitudes m_i.

2.2. F-Region Ion Velocity

Electric fields and convection velocities are related by

$$\mathbf{v}_\perp = \mathbf{E} \times \mathbf{B}/B^2, \tag{2}$$

where $\mathbf{B}$ is the magnetic field. Use of Equation 2 implies an assumption that the plasma is frozen-in. This is usually a good approximation in the upper F-region. It breaks down toward E-region altitudes where ion velocities become increasingly aligned with the neutral wind, while electrons remain frozen-in. Ion velocity measurements used in Lompe must be from a region where Equation 2 is valid. This is usually assumed to hold for SuperDARN (Chisham et al., 2007) radar measurements and ion velocity measurements from low Earth orbit satellites, such as *Swarm* (Knudsen et al., 2017) or Defense Meteorological Satellite Program (DMSP; Rich, 1994). Convection data from these and similar sources could thus easily be incorporated in the Lompe technique.

The frozen-in approximation implies that $\mathbf{B} \cdot \mathbf{E} = 0$. This equation can, in principle, be used to retrieve the vertical component of $\mathbf{E}$ if its horizontal components are specified via Equation 1. However, for simplicity we neglect terms that depend on horizontal components of the main magnetic field, and thus also any vertical component in $\mathbf{E}$. This approximation simplifies the relationship between electric currents and the magnetic field discussed below, and it leads to only small errors in polar regions (e.g., Untiedt & Baumjohann, 1993). This approximation implies that Equation 2 becomes

$$\mathbf{v}_\perp = \mathbf{E} \times \hat{\mathbf{u}} \frac{B_u}{B^2}, \tag{3}$$

where $\hat{\mathbf{u}}$ is an upward unit vector, B_u is the upward component of the magnetic field, and B is its magnitude. We believe that the effects of magnetic field inclination on polar ionospheric electrodynamics is an interesting and underexplored research topic, but it is beyond the scope of this study. Note that $\mathbf{v}_\perp$ is only the component of the velocity that is perpendicular to $\mathbf{B}$. Any parallel component should be subtracted before using Equation 3 to relate $\mathbf{v}$ and $\mathbf{E}$.

2.3. Magnetic Field Disturbances

In order to relate electric fields and conductances to magnetic field disturbances, we use the ionospheric Ohm's law integrated over the height of the ionosphere:

$$\mathbf{J} = \Sigma_P \mathbf{E}' - \Sigma_H \mathbf{E}' \times \mathbf{B}/B, \tag{4}$$

where $\mathbf{J}$ is the height-integrated electric current, which we model as a surface-current density on the spherical shell at radius R_I. $\mathbf{E}'$ is the electric field in the reference frame of the neutral wind. In the following, we make the assumption that the neutral wind is known, and skip the primes. Σ_P (P for Pedersen) and Σ_H (H for Hall) are height-integrated conductivities, referred to as conductances. Equation 4 is a steady-state solution of the set of momentum equations for ions and electrons, moving through an unaffected neutral fluid (e.g., Dreher, 1997). Only the collision and Lorentz force terms are included in the momentum equation. Inertia and all other forces are neglected. The Lompe parametrization thus assumes that these approximations are valid. Therefore, when we speak of "electrodynamics" in this manuscript, we refer to the evolution of the polar ionosphere from one quasi-steady state to another. We do not address the evolution of the ionosphere over the more rapid time scales for which Alfvénic or inductive effects are critical.

We also assume that the conductances are known. The great advantage of this is that it ensures that all other quantities can be related to the electric field model parameters by linear equations. The disadvantage is that it is difficult to know the conductances precisely. The main reason for this is the contribution to ionization from auroral precipitation, which can be highly variable and difficult to measure. The solar extreme ultraviolet (EUV) contribution to conductances is more stable. In Section 2.4, we present a novel approach to calculate solar EUV conductances, which avoids the problem of infinite gradients at the sunlight terminator that is present in some earlier work.

In its basic form, Equation 4 is not very useful to us, since we never really measure $\mathbf{J}$ directly. Instead, we measure magnetic field disturbances $\Delta\mathbf{B}$ on ground and in space. To relate $\Delta\mathbf{B}$ and $\mathbf{E}$, we calculate the magnetic field disturbances associated with $\mathbf{J}$ in Equation 4. One possible approach could be to perform a Biot-Savart integral

over a sufficiently large part of the ionospheric shell, but this would be numerically expensive. Instead, we use results from SECS analysis.

First of all, we note that Helmholtz's theorem implies that any well-behaved vector field on a 2D spherical shell can be represented as a sum of curl-free (superscript $\star$) and divergence-free (superscript $\circ$) vector fields. Consequently, we can write $\mathbf{J} = \mathbf{J}^\star + \mathbf{J}^\circ$. $\mathbf{J}^\star$ and $\mathbf{J}^\circ$ can be represented as sums of curl-free and divergence-free SECS

$$\mathbf{J}^\star(\lambda, \phi) = \sum_i \frac{-S_i^\star}{4\pi R_I} \cot\left(\frac{\pi/2 - \lambda_i}{2}\right) \hat{\mathbf{n}}_i, \tag{5}$$

$$\mathbf{J}^\circ(\lambda, \phi) = \sum_i \frac{S_i^\circ}{4\pi R_I} \cot\left(\frac{\pi/2 - \lambda_i}{2}\right) \hat{\mathbf{e}}_i, \tag{6}$$

where the summation index i is over a grid of SECS nodes (to be specified in Section 3). These basis functions are complete in that their sum can describe any 2D vector field on the sphere provided that they are placed densely enough that all relevant spatial scales are resolved. λ_i and $\hat{\mathbf{n}}_i$ have the same meaning as in Equation 1. $\hat{\mathbf{e}}_i$ is an eastward unit vector in a coordinate system with the ith SECS pole in the north pole. In practice, the vectors in Equations 5 and 6 must be expressed in a global coordinate system, in which they generally have both eastward and northward components (see Vanhamäki & Juusola, 2020, Section 2.5). The scalars $S_i^\star$ and S_i° represent the amplitudes of the ith curl-free and divergence-free basis functions, respectively.

Given the representation of $\mathbf{J}$ in terms of curl-free and divergence-free SECS, we can calculate magnetic field disturbances analytically: Amm and Viljanen (1999) showed that the magnetic field of a single curl-free SECS is (following notation from Vanhamäki and Juusola (2020), and using the colatitude $\theta = \pi/2 - \lambda$)

$$\Delta B_{n_i}(\theta_i, r) = 0, \tag{7}$$

$$\Delta B_{e_i}(\theta_i, r) = -\frac{S_i^\star \mu_0}{4\pi r} \begin{cases} 0 & r < R_I \\ \cot(\theta_i/2) & r > R_I, \end{cases} \tag{8}$$

$$\Delta B_u(\theta_i, r) = 0, \tag{9}$$

and the magnetic field of a single divergence-free SECS is

$$\Delta B_{n_i}(\theta_i, r) = \frac{\mu_0 S_i^\circ}{4\pi r \sin\theta_i} \begin{cases} \dfrac{s - \cos\theta_i}{\sqrt{1 + s^2 - 2s\cos\theta_i}} + \cos\theta_i & r < R_I \\ \dfrac{1 - s\cos\theta_i}{\sqrt{1 + s^2 - 2s\cos\theta_i}} - 1 & r > R_I \end{cases}, \tag{10}$$

$$\Delta B_{e_i}(\theta_i, r) = 0, \tag{11}$$

$$\Delta B_u(\theta_i, r) = \frac{\mu_0 S_i^\circ}{4\pi r} \begin{cases} \dfrac{1}{\sqrt{1 + s^2 - 2s\cos\theta_i}} - 1 & r < R_I \\ \dfrac{s}{\sqrt{1 + s^2 - 2s\cos\theta_i}} - s & r > R_I \end{cases}, \tag{12}$$

$$s = \min(r, R_I) / \max(r, R_I). \tag{13}$$

The magnetic field of several curl-free and divergence-free elementary current systems is the sum of the contribution from each current. These equations show how the ionospheric radius R_I, which is a user-defined parameter in our technique, affects the scaling between magnetic field perturbations and SECS amplitudes—and hence SECS currents. For a fixed set of ground magnetic field disturbances, the corresponding divergence-free current density increases with increasing R_I. For a fixed set of space magnetic field disturbances, it is opposite. One should

therefore select an R_I near the peak near the peak current layer in the ionosphere (typically the Earth radius plus 100–150 km).

Given $\mathbf{E}$, Σ_H, and Σ_P, we could use the ionospheric Ohm's law in Equation 4 to find an SECS representation of $\mathbf{J}$, and Equations 7–13 to find the associated magnetic field disturbances. However, our task here is the opposite: To find $\mathbf{E}$, given Σ_H, Σ_P, and a set of measured magnetic field disturbances. To do that, we must find a relationship between the electric field model parameters m_i (Equation 1) and the amplitudes in an SECS representation of $\mathbf{J}$.

To do this, we calculate the divergence and curl of Equation 4. Starting with the divergence, we get

$$\nabla \cdot \mathbf{J} = \nabla \cdot \mathbf{J}^{\star} = \nabla \Sigma_P \cdot \mathbf{E} + \Sigma_P \nabla \cdot \mathbf{E} \mp \hat{\mathbf{u}} \cdot (\mathbf{E} \times \nabla \Sigma_H), \tag{14}$$

where we have used the assumption $\nabla \times \mathbf{E} = 0$ made in Section 2.1. Here, $\mp$ refers to the northern $(-)$ and southern $(+)$ hemispheres due to the different orientations of the Earth's main magnetic field. This is a differential equation that relates the electric field to the curl-free part of the horizontal current. Current continuity implies that the divergence of the horizontal current is equal to the downward magnetic FAC. The combined magnetic effect of horizontal curl-free current and radial FACs is zero below the ionosphere according to Fukushima's theorem (Fukushima, 1976) and Equations 7–9.

Equation 14 is fundamental in most schemes to couple the magnetosphere with the ionosphere in global magnetohydrodynamic (MHD) simulations (e.g., Wiltberger et al., 2004). MHD simulations give the FAC density at the top of the ionosphere, which must be equal to the divergence of the horizontal ionospheric current given by Equation 14, or else charges would pile up. The resulting current continuity equation can be solved for $\mathbf{E}$, which is used as a boundary condition for the MHD simulation. In Section 3.4, we show how the Lompe framework can be used to solve the current continuity equation.

The curl-free SECS have the property that (Vanhamäki & Juusola, 2020)

$$\nabla \cdot \mathbf{J}_i^{\star} = S_i^{\star} \left(\delta(\lambda_i, \phi_i) - \frac{1}{4\pi R_I^2} \right), \tag{15}$$

where $\delta(\lambda_i, \phi_i)$ is the Dirac delta function. This property can help us to relate Equation 14 directly to a set of amplitudes $S_i^{\star}$ of SECS basis functions. To achieve this, we place the basis functions in a grid with cells denoted Ω_i. Integrating $\nabla \cdot \mathbf{J}$ over the jth cell, we obtain

$$\int_{\Omega_j} \nabla \cdot \mathbf{J} dA = \int_{\Omega_j} \nabla \cdot \sum_i \frac{S_i^{\star}}{4\pi R_I} \cot(\pi/4 - \lambda_i/2)\, \hat{\mathbf{e}}_i dA, \tag{16}$$

$$= \int_{\Omega_j} \sum_i S_i^{\star} \left(\delta(\lambda_i, \phi_i) - \frac{1}{4\pi R_I^2} \right) dA, \tag{17}$$

$$= S_j^{\star} - A_j \sum_i \frac{S_i^{\star}}{4\pi R_I^2}, \tag{18}$$

where A_j is the area of Ω_j. The sums are over all cells in a global grid. If we choose a grid with cells that are small compared to the scale size of $\mathbf{J}$, we can approximate the integral on the left-hand side to get

$$\nabla \cdot \mathbf{J}|_j A_j = S_j^{\star} - A_j \sum_i \frac{S_i^{\star}}{4\pi R_I^2}. \tag{19}$$

Equation 19 relates the divergence of $\mathbf{J}$ in Equation 14, evaluated on a discrete set of points, to the amplitudes $S_i^{\star}$. These amplitudes are in turn related to the magnetic field disturbances via the equations presented above. This relationship can then be used to find a linear relationship between magnetic field disturbances associated with curl-free currents and the electric field model parameters m_i. In Section 3, we introduce our choice of grid and describe how we use Equation 19 to construct matrix equations that relate magnetic and electric fields.

The other part of the magnetic field relates to divergence-free currents. We calculate the curl of the ionospheric Ohm's law to get an expression that only depends on this part of the current

$$(\nabla \times \mathbf{J})_u = (\nabla \times \mathbf{J}^\circ)_u = \nabla\Sigma_P \times \mathbf{E} \mp (\nabla\Sigma_H \cdot \mathbf{E})\,\hat{\mathbf{u}} \mp \Sigma_H(\nabla \cdot \mathbf{E})\hat{\mathbf{u}}, \tag{20}$$

again using the assumption that $\nabla \times \mathbf{E} = 0$. This is a differential equation that relates the electric field to the divergence-free part of the current. The divergence-free current is often treated as synonymous with the so-called equivalent current (e.g., Laundal et al., 2015), a theoretical 2D current in the ionosphere that is equivalent with magnetic field disturbances on the ground. Equation 20 is the foundation of the KRM technique (Kamide et al., 1981) which is used to infer ionospheric electrodynamic parameters from ground magnetometer measurements. We use the same principle here, applied to SECS instead of the spherical harmonic representation used by Kamide et al. (1981), or the spherical cap harmonic representation used in AMIE (Richmond & Kamide, 1988). Vanhamäki and Amm (2007) were the first to use the KRM technique with SECS, but their approach is different from what we propose here.

The divergence-free SECS have the property that

$$\left(\nabla \times \mathbf{J}_i^\circ\right)_u = S_i^\circ \left(\delta(\lambda_i, \phi_i) - \frac{1}{4\pi R_I^2}\right). \tag{21}$$

Following the same procedure as with $\nabla \cdot \mathbf{J}$, integrating over the grid cell Ω_j, we find that

$$(\nabla \times \mathbf{J})_u|_j\, A_j = S_j^\circ - A_j \sum_i \frac{S_i^\circ}{4\pi R_I^2}, \tag{22}$$

which will be used in Section 3, together with Equation 19, to find matrix equations that relate magnetic field measurements to the electric field model parameters m_i.

2.4. Solar EUV Conductances

The Lompe technique requires that ionospheric conductances are known. The conductance is a sum of contributions from precipitation by ionizing particles (auroral conductance) and ionization by solar EUV radiation. Many empirical formulas for the solar EUV contribution to ionospheric Pedersen and Hall conductances, hereafter Σ_P^{EUV} and Σ_H^{EUV}, express this contribution as a function of the solar zenith angle χ that is proportional to $\cos\chi$ or a linear combination of powers thereof (Ieda et al., 2014). The underlying assumption is that Σ_P^{EUV} and Σ_H^{EUV} are related to the maximum ionospheric plasma production along the path traveled by solar radiation (i.e., along the line defined by a particular value of χ). The maximum ionospheric plasma production for a particular species is, in turn, proportional to $\cos\chi$ under some simplifying assumptions, including that (i) the neutral atmosphere is vertically stratified (i.e., the earth is flat), and (ii) the neutral atmosphere density height profile is exponential (e.g., Ieda et al., 2014; Schunk & Nagy, 2009).

For our purposes, the chief shortcoming of these formulations is that the derivatives of Σ_P^{EUV} and Σ_H^{EUV} are discontinuous at $\chi = 90°$. We have therefore developed an alternative procedure for calculating Σ_P^{EUV} and Σ_H^{EUV} by instead assuming that the neutral atmosphere is radially rather than vertically stratified (i.e., the earth is round). In summary, setting to zero the derivative of the plasma production function (e.g., Equation 9.21 in Schunk and Nagy (2009))

$$q(z, \chi) = q_0 n(z)\, e^{-\tau(z,\chi)} \tag{23}$$

with respect to altitude z yields the transcendental equation

$$\frac{d}{dz}\left[e^{-(z-z_0)/H}\mathrm{Ch}(z, \chi)\right] = -\frac{1}{\sigma H^2 n_0}, \tag{24}$$

which can be solved numerically to obtain the height of maximum plasma production $z_m(\chi)$ for a given value of χ. In the preceding equations, $\tau(z, \chi)$ is the optical depth, $n(z) = n_0 e^{-(z-z_0)/H}$ is the atmospheric neutral density profile, H is a constant scale height, σ is the absorption cross section, and

$$\mathrm{Ch}(z, \chi) = \frac{1}{H}\int_z^\infty e^{-(z'-z)/H}\left[1 - \left(\frac{R_E + z}{R_E + z'}\right)^2 \sin^2\chi\right]^{-1/2} dz' \tag{25}$$

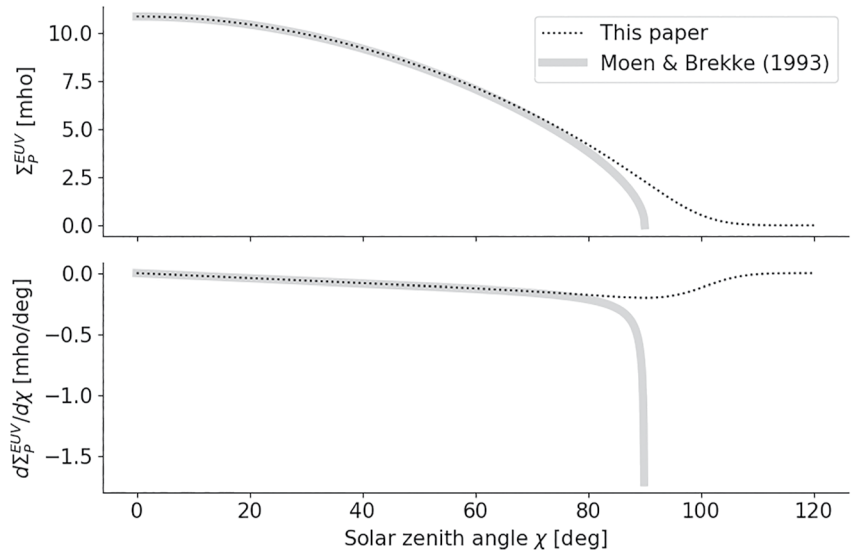

Figure 2. Solar extreme ultraviolet (EUV) contribution to Pedersen conductance (top) and its derivative (bottom) calculated using Equation 28 (thick gray line) and Equation 6 in Moen and Brekke (1993) (dotted black line). Here, $z_m(\chi)$ in Equation 28 is calculated by solving Equation 24 with $n_0 = 10^{13}$ m^{-3}, $z_0 = 500$ km, $H = 50$ km, and absorption cross section $\sigma = 10^{-20}$ m^2.

is the Chapman function (e.g., Huestis, 2001). We then calculate the relative maximum production

$$q'(\chi) = \frac{q\left(z_m(\chi),\, \chi\right)}{q\left(z_m\left(0°\right), 0°\right)} \tag{26}$$

for all χ in [0°, 120°].

The function $q'(\chi)$ is directly analogous to $\cos\chi$, such that $q'(\chi) \to \cos\chi$ as $R_E \to \infty$ in Equation 25. To calculate Σ_P^{EUV} and Σ_H^{EUV} in the Lompe model we therefore replace $\cos\chi$ with $q'(\chi)$ in the empirical formulas presented by Moen and Brekke (1993)

$$\Sigma_H^{\text{EUV}} = \text{F10.7}^{0.53}\left(0.81q'(\chi) + 0.54\sqrt{q'(\chi)}\right); \tag{27}$$

$$\Sigma_P^{\text{EUV}} = \text{F10.7}^{0.49}\left(0.34q'(\chi) + 0.93\sqrt{q'(\chi)}\right). \tag{28}$$

Figure 2 shows Σ_P^{EUV} both as given by Equation 6 in Moen and Brekke (1993) and as given here in Equation 28, as well as their derivatives with respect to χ.

3. Numerical Implementation

In this section, we present how we formulate the theory of Section 2 in terms of matrix equations that relate the electric field model parameters m_i in Equation 1 to measurements of the electric field, ionospheric convection, ground magnetic field disturbances, and space magnetic field disturbances. We start by introducing the grid, before we go through the matrix equations for each type of measurement. In Section 3.3, we discuss how the resulting set of equations is solved.

3.1. The Grid

The basis of the matrix formulations below is a regular grid in a cubed-sphere projection (Ronchi et al., 1996). We model the ionosphere as a 2D spherical shell at radius R_I, and the cubed-sphere projection maps every point of the sphere onto a circumscribed cube by extending the line that connects the center of the Earth and the position on the sphere until it intersects the cube. To minimize distortion, we rotate the cube such that one of the faces

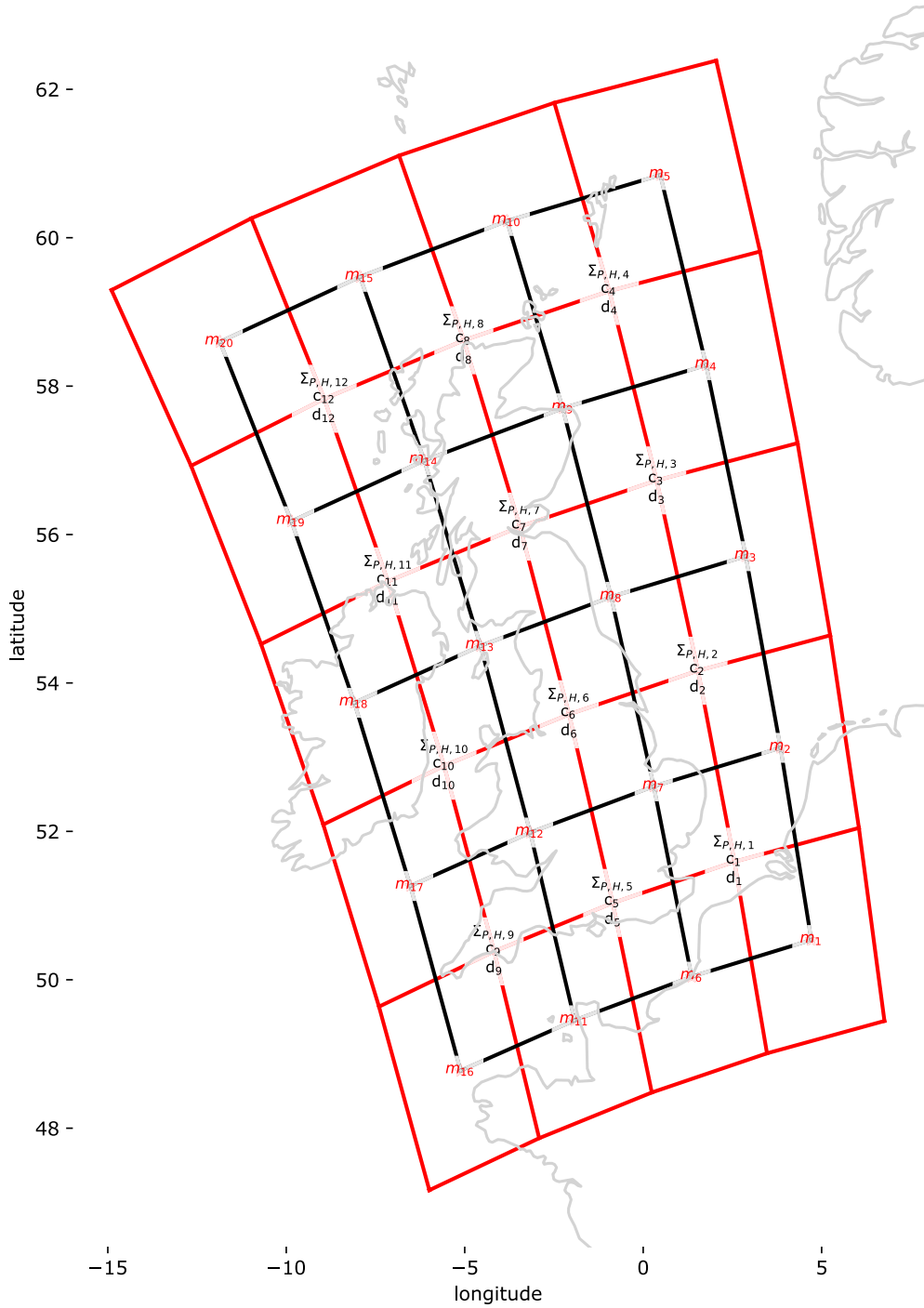

Figure 3. Example of the cubed-sphere grid used in Lompe, in this case covering the British Isles. For illustration purposes, this grid is much coarser than the grids used for actual calculations. Shown in a cylindrical projection.

intersects the center of our region of interest. In our current implementation, we use only coordinates on this intersecting cube face.

Figure 3 shows an example grid in red, with electric field SECS poles with amplitudes m_i (Equation 1) at the center of each cell. This example grid is intentionally very coarse for illustration purposes; in reality it can be placed at any location, with any orientation, aspect ratio, and resolution. It can cover regions of any size as long as all points map to a single cube face.

Figure 3 also shows an interior grid, in black, whose cells are centered on the inner vertices of the red grid. As will be explained in more detail below, these points are where the divergence (labeled d_i in the figure) and curl (labeled c_i) of $\mathbf{J}$ will be evaluated in order to relate m_i to magnetic field measurements. The outer grid has K_E grid cells and the inner cell has K_J grid cells. In this example, $K_E = 20$ and $K_J = 12$.

Before we proceed, we note that the relationships between $\mathbf{E}$ (expressed in terms of m_i) and the curl/divergence of $\mathbf{J}$ involve horizontal gradients of Σ_H and Σ_P. We therefore introduce $K_J \times K_J$ matrices $\mathbb{D}_{\mathbf{e}\cdot\nabla}$ and $\mathbb{D}_{\mathbf{n}\cdot\nabla}$ (we use this "blackboard-bold" notation for matrices throughout the paper) which produces the eastward and northward components of the gradient of a scalar field defined on the inner K_J grid cells. That is, if $\mathbf{\Sigma}_H$ is a $K_J \times 1$ vector containing the values of Σ_H at the centers of the inner grid cells, $\mathbb{D}_{\mathbf{e}\cdot\nabla}\mathbf{\Sigma}_H$ yields another $K_J \times 1$ vector with $\hat{\mathbf{e}} \cdot \nabla\Sigma_H$ evaluated at the same points. The differentiation is carried out using a finite difference scheme, and the elements of the differentiation matrices depend on the stencil used, distortion effects to take into account Earth's spherical shape (Ronchi et al., 1996), and on the orientation and position of the grid with respect to the underlying global coordinate system.

Equations 14 and 20 also involve the divergence of $\mathbf{E}$ itself. We therefore also define a $K_J \times 2K_J$ matrix $\mathbb{D}_{\nabla\cdot}$, which calculates the divergence of $\mathbf{E}$ evaluated at the center of the K_J grid cells. This matrix is also implemented using a finite difference scheme. In Section 3.2.1, it will be made clearer how this matrix is used.

The SECS definitions include a cot function that approaches infinity toward the node. This singularity is a main reason why we use two grids that are offset from each other. For example, we evaluate the curl and divergence of $\mathbf{J}$ at the centers of the inner grid cells, away from the electric field nodes. Our data points, however, are not necessarily optimally placed with respect to the nodes. We handle this by modifying the SECS function definitions near the node as proposed by Vanhamäki and Juusola (2020). The modification is applied in regions that are closer to an SECS pole than half a grid cell extent.

3.2. Matrix Formulation

The model parameters, the electric field SECS amplitudes m_i, are organized in a $K_E \times 1$ vector $\mathbf{m}$. We use the notation $\tilde{\mathbf{y}}$ to denote an $N \times 1$ vector of N predictions of some general quantity y, in practice either the electric field, F-region ion velocity, ground magnetic field perturbation, or space magnetic field perturbation. In the following subsections, we go through the matrices that relate each of these quantities to the model vector $\mathbf{m}$. Our aim is to describe the $N \times K_E$ matrix $\mathbb{G}$ in the linear system

$$\tilde{\mathbf{y}} = \mathbb{G}\mathbf{m}, \tag{29}$$

which relates $\tilde{\mathbf{y}}$ and $\mathbf{m}$. This section (Section 3.2) describes the forward problem, how to calculate $\mathbb{G}$. Section 3.3 describes how we solve the inverse problem: Finding $\mathbf{m}$ given a set of measurements $\tilde{\mathbf{y}}$.

3.2.1. Electric Field

As described in Section 2.1, the electric field is represented as a sum of curl-free SECS with amplitudes m_i, $i = 1, 2, \ldots, K_E$, forming the elements of the vector $\mathbf{m}$. We can relate N_E predictions of the electric field eastward and northward components to $\mathbf{m}$ via a $2N_E \times K_E$ system of equations

$$\begin{pmatrix} \tilde{\mathbf{E}}_e \\ \tilde{\mathbf{E}}_n \end{pmatrix} = \begin{pmatrix} \mathbb{E}_e \\ \mathbb{E}_n \end{pmatrix} \mathbf{m}, \tag{30a}$$

$$\tilde{\mathbf{E}} = \mathbb{E}\mathbf{m}, \tag{30b}$$

where $\tilde{\mathbf{E}}_e$ and $\tilde{\mathbf{E}}_n$ are $N_E \times 1$ column vectors with eastward and northward electric field components, stacked to form the $2N_E \times 1$ vector $\tilde{\mathbf{E}}$. $\mathbb{E}_e$ is a $N_E \times K_E$ matrix whose jth row relates the jth element of $\tilde{\mathbf{E}}_e$ to $\mathbf{m}$. The elements of this row are the terms in the sum in Equation 1, projected on the eastward unit vector. That is, the (j, i)th element of $\mathbb{E}_e$ is

$$\mathbb{E}_{e_{j,i}} = \frac{-1}{4\pi R_I} \cot\left(\frac{\pi/2 - \lambda_{j,i}}{2}\right) \hat{\mathbf{n}}_{j,i} \cdot \hat{\mathbf{e}}, \tag{31}$$

where $\lambda_{j,i}$ is the latitude of the jth element in $\tilde{\mathbf{E}}_e$, expressed in a local coordinate system where the ith SECS node is at the north pole. $\hat{\mathbf{n}}_{j,i}$ is a unit vector pointing tangentially to the sphere from the jth prediction to the ith SECS node (a northward unit vector in the coordinate system centered on the ith node). $\mathbb{E}_n$ is defined analogously, relating the northward components to $\mathbf{m}$.

3.2.2. Velocity

The velocity is related to the electric field via Equation 3, given the assumptions outlined in Section 2.2. Equation 3 includes the magnetic field, which is strongly dominated by sources internal to the Earth, the "main magnetic field," described by the International Geomagnetic Reference Field (IGRF; Alken et al., 2021). Let $\mathbb{B}_0$ be an $N_v \times N_v$ diagonal matrix formed by B_u/B^2, where B_u is the upward component and B is the total magnitude of the main field at N_v velocity vector locations. N_v predictions of the eastward and northward components of the velocity are related to $\mathbf{m}$ via a $2N_v \times K_E$ system of equations

$$\begin{pmatrix} \tilde{\mathbf{v}}_e \\ \tilde{\mathbf{v}}_n \end{pmatrix} = \begin{pmatrix} \mathbb{V}_e \\ \mathbb{V}_n \end{pmatrix} \mathbf{m}, \tag{32a}$$

$$= \begin{pmatrix} \mathbb{B}_0 & \mathbb{0} \\ \mathbb{0} & \mathbb{B}_0 \end{pmatrix} \begin{pmatrix} \mathbb{E}_n \\ -\mathbb{E}_e \end{pmatrix} \mathbf{m}, \tag{32b}$$

$$\tilde{\mathbf{v}} = \mathbb{V}\mathbf{m}, \tag{32c}$$

where $\mathbb{0}$ is an $N_v \times N_v$ zero matrix. Here, $\mathbb{V}_e$, $\mathbb{V}_n$, $\mathbb{E}_e$, and $\mathbb{E}_n$ are $N_v \times K_E$ matrices.

Very often the ion velocity is only measured along one direction. For example, SuperDARN gives measurements of $\mathbf{v}$ along the line-of-sight direction of the radars. If we have N_v line-of-sight measurements, the matrix $\mathbb{V}_{\text{los}}$, which relates the line-of-sight measurements to $\mathbf{m}$, has dimensions $N_v \times K_E$ and can be expressed in terms of unit vectors in the line-of-sight direction, $\mathbf{l} = l_e\mathbf{e} + l_n\mathbf{n}$

$$\tilde{\mathbf{v}}_{\text{los}} = \mathbb{V}_{\text{los}}\mathbf{m} = \mathbb{B}_0 \left(\mathbb{l}_e\mathbb{E}_n - \mathbb{l}_n\mathbb{E}_e\right)\mathbf{m}, \tag{33}$$

where $\mathbb{l}_e$ and $\mathbb{l}_n$ are $N_v \times N_v$ diagonal matrices formed by the N_v line-of-sight vector components l_e and l_n, respectively. Equation 33 allows us to use line-of-sight convection measurements to constrain the velocity field implied by $\mathbf{m}$ without any assumption about the perpendicular component.

3.2.3. Ground Magnetic Field

As discussed in Section 2.3, the combined magnetic field of FACs and curl-free currents cancel on ground, so only the divergence-free currents are relevant when modeling ground magnetic field perturbations.

In this classical application of SECS, the divergence-free part of the horizontal ionospheric current is represented as a weighted sum of elementary currents, Equation 6, and ground magnetic field disturbances are related to these currents via Equations 10–12. Let $\mathbf{S}^\circ$ be a $K_J \times 1$ vector of divergence-free SECS amplitudes, defined on the K_J interior grid points. We can write the relationship between $\mathbf{S}^\circ$ and a set of ground magnetic field disturbance vector components $\Delta\tilde{\mathbf{B}}_{ge}$, $\Delta\tilde{\mathbf{B}}_{gn}$, and $\Delta\tilde{\mathbf{B}}_{gu}$ (subscripts referring to east, north, up) as

$$\begin{pmatrix} \Delta\tilde{\mathbf{B}}_{ge} \\ \Delta\tilde{\mathbf{B}}_{gn} \\ \Delta\tilde{\mathbf{B}}_{gu} \end{pmatrix} = \begin{pmatrix} \mathbb{H}^\circ_{ge} \\ \mathbb{H}^\circ_{gn} \\ \mathbb{H}^\circ_{gu} \end{pmatrix} \mathbf{S}^\circ, \tag{34a}$$

$$\Delta\tilde{\mathbf{B}}_g = \mathbb{H}^\circ_g\mathbf{S}^\circ, \tag{34b}$$

where the elements of the matrices $\mathbb{H}^{\circ}_{ge}$, $\mathbb{H}^{\circ}_{gn}$, and $\mathbb{H}^{\circ}_{gu}$ are given by Equations 10–12. With a total of N_{B_g} 3D vector predictions, $\mathbb{H}^{\circ}_{g}$ has shape $3N_{B_g} \times K_J$.

Our aim is to relate the magnetic field vector components to the electric field model vector $\mathbf{m}$. To do that, we use the curl of the ionospheric Ohm's law, Equation 20. We define a column vector $\mathbf{c}$ formed by the curl of the ionospheric current evaluated at the center of the K_J interior grid points. Equation 22 can be used to construct a matrix equation that relates $\mathbf{c}$ and $\mathbf{S}^{\circ}$

$$\mathbb{A}\mathbf{c} = \mathbb{Q}\mathbf{S}^{\circ}, \tag{35}$$

where $\mathbb{A}$ is a $K_J \times K_J$ diagonal matrix formed by the areas of the K_J cells. $\mathbb{Q}$ is a $K_J \times K_J$ matrix with elements

$$Q_{ji} = \delta_{ji} - A_{jj}/4\pi R_I^2, \tag{36}$$

where δ_{ji} is the Kronecker delta, defined to be 0 when $j \neq i$ and 1 when $j = i$, not to be confused with the Dirac delta function used in Equations 15 and 21.

The last term in Equation 36 comes from the sum in Equation 22. This sum is the contribution to the curl in the jth cell (i.e., Ω_j) from all elementary current systems. In theory, this should include current systems that are outside our grid. We ignore this here, noting that their contributions to the curl are scaled by a very small number: The area of the local grid cell A_{jj} divided by the total area of the sphere. Their net amplitude would have to be very large to make a significant contribution to the curl in cell Ω_j.

Equations 34b and 35 can be combined to give

$$\Delta\tilde{\mathbf{B}}_g = \mathbb{H}^{\circ}_{g}\mathbb{Q}^{-1}\mathbb{A}\mathbf{c}. \tag{37}$$

The vector $\mathbf{c}$ can be expressed in terms of the electric field model vector $\mathbf{m}$ by using Equation 20

$$\begin{aligned}\mathbf{c} = \big[&-\mathrm{diag}\left(\mathbb{D}_{\hat{\mathbf{n}}\cdot\nabla}\boldsymbol{\Sigma}_P\right)\mathbb{E}_e + \mathrm{diag}\left(\mathbb{D}_{\hat{\mathbf{e}}\cdot\nabla}\boldsymbol{\Sigma}_P\right)\mathbb{E}_n \\ &\mp\mathrm{diag}\left(\mathbb{D}_{\hat{\mathbf{n}}\cdot\nabla}\boldsymbol{\Sigma}_H\right)\mathbb{E}_n \mp \mathrm{diag}\left(\mathbb{D}_{\hat{\mathbf{e}}\cdot\nabla}\boldsymbol{\Sigma}_H\right)\mathbb{E}_e \\ &\mp\mathrm{diag}\left(\boldsymbol{\Sigma}_H\right)\mathbb{D}_{\nabla\cdot}\mathbb{E}\big]\,\mathbf{m} = \mathbb{c}\mathbf{m},\end{aligned} \tag{38}$$

where the "diag" function produces a diagonal matrix with the elements of the argument vector on the diagonal. $\boldsymbol{\Sigma}_H$ and $\boldsymbol{\Sigma}_P$ are $K_J \times 1$ column vectors that contain the Hall and Pedersen conductances, respectively, in the K_J interior grid cells. Recall that the matrices $\mathbb{D}_{\hat{\mathbf{e}}\cdot\nabla}$ and $\mathbb{D}_{\hat{\mathbf{n}}\cdot\nabla}$, multiplied by $\boldsymbol{\Sigma}_H$, produces K_J values of the gradient of the Hall conductance in the eastward and northward directions, respectively.

In Equation 38, $\mathbb{E}$ is a $2K_J \times K_E$ matrix composed of the two $K_J \times K_E$ block matrices $\mathbb{E}_e$ and $\mathbb{E}_n$ that map the K_E electric field SECS amplitudes in $\mathbf{m}$ to K_J values of eastward and northward electric field components at the centers of the interior grid cells. With this definition, the divergence matrix $\mathbb{D}_{\nabla\cdot}$ from Section 3.1 can be used to directly map $\mathbf{m}$ to the electric field divergences at the centers of the K_J interior grid cells: $\mathbb{D}_{\nabla\cdot}\mathbb{E}\mathbf{m}$.

The sum of all the terms in square brackets is a $K_J \times K_E$ matrix $\mathbb{c}$. This gives the following relationship between $\Delta\tilde{\mathbf{B}}_g$ and $\mathbf{m}$

$$\begin{aligned}\Delta\tilde{\mathbf{B}}_g &= \mathbb{H}^{\circ}_{g}\mathbb{Q}^{-1}\mathbb{A}\mathbb{c}\mathbf{m} \\ &= \mathbb{B}^{\circ}_{g}\mathbf{m} = \mathbb{B}_g\mathbf{m}.\end{aligned} \tag{39}$$

The divergence-free SECS amplitudes $\mathbf{S}^{\circ}$ are not directly involved in Equation 39, but can be calculated if needed by combining Equations 35 and 39

$$\mathbf{S}^{\circ} = \mathbb{Q}^{-1}\mathbb{A}\mathbb{c}\mathbf{m}. \tag{40}$$

3.2.4. Space Magnetic Field

The magnetic field in space is often assumed to be dominated by the curl-free part of the ionospheric current system, including the FACs which represents its divergence. If this assumption is true, the magnetic field in space can be related to a set of K_J curl-free currents with amplitudes $\mathbf{S}^\star$ via Equation 5

$$\begin{pmatrix} \Delta\tilde{\mathbf{B}}_e^\star \\ \Delta\tilde{\mathbf{B}}_n^\star \\ \Delta\tilde{\mathbf{B}}_u^\star \end{pmatrix} = \begin{pmatrix} \mathbb{H}_e^\star \\ \mathbb{H}_n^\star \\ \mathbb{H}_u^\star \end{pmatrix} \mathbf{S}^\star, \tag{41a}$$

$$\Delta\tilde{\mathbf{B}}^\star = \mathbb{H}^\star \mathbf{S}^\star. \tag{41b}$$

The first step in relating $\mathbf{S}^\star$ to the model vector $\mathbf{m}$ is to relate it to the divergence of the ionospheric Ohm's law. Let $\mathbf{d}$ be a column vector with the divergence of the current evaluated in the center of the K_J interior grid cells. Equation 19 gives the following relationship:

$$\mathbb{A}\mathbf{d} = \mathbb{Q}\mathbf{S}^\star, \tag{42}$$

where $\mathbb{A}$ and $\mathbb{Q}$ are the same as in Equation 35.

The vector $\mathbf{d}$, the divergence of the electric current evaluated in the interior grid cells, can be expressed from the divergence of the ionospheric Ohm's law, Equation 14

$$\begin{aligned} \mathbf{d} = \big[& \mp \mathrm{diag}\left(\mathbb{D}_{\hat{\mathbf{n}}\cdot\nabla}\boldsymbol{\Sigma}_H\right)\mathbb{E}_e \pm \mathrm{diag}\left(\mathbb{D}_{\hat{\mathbf{e}}\cdot\nabla}\boldsymbol{\Sigma}_H\right)\mathbb{E}_n \\ & + \mathrm{diag}\left(\mathbb{D}_{\hat{\mathbf{e}}\cdot\nabla}\boldsymbol{\Sigma}_P\right)\mathbb{E}_e + \mathrm{diag}\left(\mathbb{D}_{\hat{\mathbf{n}}\cdot\nabla}\boldsymbol{\Sigma}_P\right)\mathbb{E}_n \\ & + \mathrm{diag}\left(\boldsymbol{\Sigma}_P\right)\mathbb{D}_{\nabla\cdot}\mathbb{E}\big]\,\mathbf{m} = \mathbb{d}\mathbf{m}, \end{aligned} \tag{43}$$

where $\mathbb{E}_e$, $\mathbb{E}_n$, and $\mathbb{E}$ are defined as in Equation 38. Now we can combine Equations 41b, 42, and 43 to find a matrix $\mathbb{B}^\star$ that relates the magnetic field of curl-free currents to the model vector $\mathbf{m}$

$$\Delta\tilde{\mathbf{B}}^\star = \mathbb{H}^\star\mathbb{Q}^{-1}\mathbb{A}\mathbb{d}\mathbf{m} = \mathbb{B}^\star\mathbf{m}. \tag{44}$$

This set of equations is quite often sufficient to model magnetic field perturbations in space, especially when observed at high altitudes. However, satellites in lower orbits, like *Swarm*, also sense the magnetic field of the divergence-free currents (Laundal et al., 2016). In that case, the full magnetic field is a sum of two contributions. We get

$$\Delta\tilde{\mathbf{B}} = \Delta\tilde{\mathbf{B}}^\circ + \Delta\tilde{\mathbf{B}}^\star = \left(\mathbb{H}_s^\circ\mathbb{Q}^{-1}\mathbb{A}\mathbb{c} + \mathbb{H}^\star\mathbb{Q}^{-1}\mathbb{A}\mathbb{d}\right)\mathbf{m} = \left(\mathbb{B}_s^\circ + \mathbb{B}^\star\right)\mathbf{m} = \mathbb{B}_s\mathbf{m}, \tag{45}$$

where the matrix $\mathbb{H}_s^\circ$ is analogous to $\mathbb{H}_g^\circ$ from Equation 39, except that it is calculated with the versions of Equations 10–12 for $r > R_I$.

3.2.5. The Full Forward Model

Equations 30b, 32c, 39, and 45 relate model predictions of the electric field, F-region plasma velocity, ground magnetic field perturbations, and space magnetic field perturbations, to the same set of model parameters, $\mathbf{m}$. The full set of linear equations can be written as

$$\begin{pmatrix} \tilde{\mathbf{E}} \\ \tilde{\mathbf{v}} \\ \tilde{\mathbf{B}}_g \\ \tilde{\mathbf{B}}_s \end{pmatrix} = \tilde{\mathbf{y}} = \begin{pmatrix} \mathbb{E} \\ \mathbb{V} \\ \mathbb{B}_g \\ \mathbb{B}_s \end{pmatrix} \mathbf{m} = \mathbb{G}\mathbf{m}. \tag{46}$$

$\mathbb{G}$ has dimensions $\left(2N_E + 2N_v + 3N_{B_g} + 3N_{B_s}\right) \times K_E$, possibly with fewer rows if not all vector components are calculated. $\mathbb{G}$ depends on the conductance and on the geometry of the problem: The choice of grids, and the coordinates of the model predictions $\tilde{\mathbf{y}}$. When $\mathbf{m}$ is known, all the parameters on the left-hand side of Equation 46 can be estimated at any location within the analysis region.

3.3. Inversion

Here, we describe our approach for solving the set of Equation 46 for $\mathbf{m}$, given a set of measurements $\tilde{\mathbf{y}}$. Naively, this could be done by minimizing the sum of squared errors, which can be written as

$$\chi^2 = (\tilde{\mathbf{y}} - \mathbb{G}\mathbf{m})^\top (\tilde{\mathbf{y}} - \mathbb{G}\mathbf{m}) . \tag{47}$$

However, there are several problems with this, which we outline below, along with our approach to solve them.

First, in SI units the magnetic field variance σ_B^2 is several orders of magnitude less than the electric field variance σ_E^2, and even less than the convection velocity variance σ_v^2. If we formulate the equations in SI units, which we do in our implementation, the misfit will be dominated by convection velocities. If we just minimize χ^2, any magnetic field measurement would be practically neglected because of this mismatch. We solve this problem by scaling χ^2 using the matrix $\mathbb{C}$

$$\chi^2 = (\tilde{\mathbf{y}} - \mathbb{G}\mathbf{m})^\top \mathbb{C} (\tilde{\mathbf{y}} - \mathbb{G}\mathbf{m}) , \tag{48}$$

where the diagonal elements of $\mathbb{C}$ are $w_i/(\sigma_B + \epsilon_i)^2$, $w_i/(\sigma_v + \epsilon_i)^2$, or $w_i/(\sigma_E + \epsilon_i)^2$, depending on which measurement that element corresponds to. Here, ϵ_i is the measurement error of the ith data point. For example, if $\sigma_B = 100$ nT, equations that involve *Swarm* magnetometer data (sub-nT precision) would be weighted by $w_i/\left(100 \cdot 10^{-9}\right)^2$, while an Iridium data point with, say, 50 nT error would be weighted by $w_i/\left(150 \cdot 10^{-9}\right)^2$.

Second, the measurements are almost always highly nonuniformly located. If no correction is applied, we risk that an isolated good data point is overshadowed because of a nearby cluster of data points. Our solution to this problem is to introduce spatial weights w_i, defined as 1 divided by the number of measurements in the grid cell in which the measurement belongs.

Finally, even with these adjustments to the cost function (Equation 48), the inverse problem is almost always ill-posed. The reason for this is that the number, type, and distribution of measurements rarely is sufficient to robustly determine $\mathbf{m}$. This leads to overfitting and large variations in $\mathbf{m}$ for small changes in the measurements. We solve this by adding a priori information to the cost function. Specifically, we (i) add a penalty for large model vectors to ensure relatively smooth spatial structures and (ii) add a penalty for large gradients in m_i in the magnetic eastward direction. The latter is justified by the fact that auroral electrodynamics tends to be aligned in the magnetic east-west direction. However, in the polar cap, poleward of the auroral oval, this constraint may be less suitable. We can control the balance between the two constraints using two regularization parameters λ_1' and λ_2'. The total cost function is then

$$f = (\tilde{\mathbf{y}} - \mathbb{G}\mathbf{m})^\top \mathbb{C} (\tilde{\mathbf{y}} - \mathbb{G}\mathbf{m}) + \lambda_1' \|\mathbf{m}\|^2 + \lambda_2' \|\mathbb{D}_{\hat{\mathbf{e}}_m \cdot \nabla}\mathbf{m}\|^2, \tag{49}$$

where $\mathbb{D}_{\hat{\mathbf{e}}_m \cdot \nabla}$ is a $K_E \times K_E$ differentiation matrix, as defined in Section 3.1, except that it gives the gradient in the *magnetic* eastward direction. We seek the model vector $\mathbf{m}$ that minimizes f. This can be found by solving the equation $\partial f/\partial \mathbf{m} = 0$ for $\mathbf{m}$. The solution is

$$\mathbf{m} = \left(\mathbb{G}^\top \mathbb{C}\mathbb{G} + \lambda_1' \mathbb{I} + \lambda_2' \mathbb{D}_{\hat{\mathbf{e}}_m \cdot \nabla}^\top \mathbb{D}_{\hat{\mathbf{e}}_m \cdot \nabla}\right)^{-1} \left(\mathbb{G}^\top \mathbb{C}\tilde{\mathbf{y}}\right) , \tag{50}$$

where $\mathbb{I}$ is the $K_E \times K_E$ identity matrix. Since the magnitude of the elements in $\mathbb{G}^\top\mathbb{C}\mathbb{G}$ depends on the amount of data, λ_1' and λ_2' must be different in different events even with the same degree of regularization. To make the numbers more comparable between events, we will instead refer to the unprimed λ_1 and λ_2, which relate to the primed variables as

$$\lambda_1' = \alpha_1 \lambda_1, \qquad \lambda_2' = \alpha_2 \lambda_2, \tag{51}$$

where α_1 is the median diagonal element of $\mathbb{G}^\top\mathbb{C}\mathbb{G}$, and α_2 is the same number divided by the median diagonal element of $\mathbb{D}^\top_{\hat{\mathbf{e}}_m\cdot\nabla}\mathbb{D}_{\hat{\mathbf{e}}_m\cdot\nabla}$. This normalization ensures that if λ_1 and λ_2 are 1, the corresponding scaled regularization matrices will have elements that are of similar magnitude as the diagonal elements in $\mathbb{G}^\top\mathbb{C}\mathbb{G}$. In this paper, we find a suitable set of regularization parameters by visual inspection, looking for (approximately) the smallest possible values that prevent overfitting. A more unbiased approach would be preferable, and we will explore different methods in future studies.

This regularization technique was also used in the Observing System Simulation Experiment carried out for the EZIE (Laundal et al., 2021), an NASA mission planned for launch in 2024. We plan to explore alternative methods in future applications of the Lompe technique. For example, instead of damping variation in the magnetic east-west direction, more complex spatial structures could be promoted by changing the regularization matrix accordingly. For example, one could use the spatial structure of empirical models or, as demonstrated by Clayton et al. (2019) with a different technique, use auroral images to derive the dominant direction of variation. It could also be possible to vary the regularization across the grid, in order to resolve fine-scale structures in regions with particularly high data density.

3.4. Solving the Current Continuity Equation

Before we present example applications, we mention an alternative use of the matrices described above: Solving the current continuity equation for the electric field, given a pattern of vertical currents. As mentioned in Section 2, this is a standard way to couple global MHD simulations of the magnetosphere to the ionosphere. The upward current density, from the MHD simulation, is set equal to the negative divergence of the horizontal ionospheric current (Equation 14), and the resulting equation is solved for the electric field, which then serves as the inner boundary condition for the magnetosphere simulation.

With the matrices defined above, we can formulate the following matrix equation relating electric field amplitudes $\mathbf{m}$ and vertical current densities $\tilde{\mathbf{j}}_\mathbf{u}$

$$\tilde{\mathbf{j}}_\mathbf{u} = \mathbb{D}_{\nabla\cdot}\left[\begin{pmatrix} \mathrm{diag}\,(\boldsymbol{\Sigma}_P)\,\mathbb{E}_e \\ \mathrm{diag}\,(\boldsymbol{\Sigma}_P)\,\mathbb{E}_n \end{pmatrix} + \begin{pmatrix} \pm\mathrm{diag}\,(\boldsymbol{\Sigma}_H)\,\mathbb{E}_n \\ \mp\mathrm{diag}\,(\boldsymbol{\Sigma}_H)\,\mathbb{E}_e \end{pmatrix}\right]\mathbf{m}, \tag{52}$$

where, as earlier, the two signs apply to the northern (top) and southern (bottom) hemispheres. The quantity in square brackets, when multiplied by $\mathbf{m}$, gives the sum of Pedersen and Hall current densities defined on the K_J interior grid points, with the eastward components stacked on top of the northward components. The matrix in square brackets has shape $2K_J \times K_E$. $\mathbb{D}_{\nabla\cdot}$ has shape $K_J \times 2K_J$ as before.

In this equation, unlike Equation 46, the data vector on the left-hand side, $\tilde{\mathbf{j}}_\mathbf{u}$, does not represent measurements at arbitrary positions, but specifically K_J vertical current densities at the internal grid points. In theory, the right-hand side could be multiplied by an appropriate interpolation matrix to relate vertical current densities at arbitrary positions to $\mathbf{m}$.

In the current form, given a set of vertical currents across the analysis domain, Equation 52 can be inverted to find $\mathbf{m}$, and thus the electric field. The electric potential, convection velocity, horizontal current densities, and magnetic field disturbances at any altitude can then be calculated from the equations presented earlier in this section. Below we demonstrate this with FAC densities from an MHD simulation. AMPERE FACs can also be used as input for this procedure, as recently demonstrated by Robinson et al. (2021) and Chartier et al. (2022), using two different techniques.

3.5. Note About Coordinate Systems

In our implementation of the Lompe technique we use geographic coordinates by default. This is because geographic coordinates are orthogonal, unlike some magnetic coordinate systems (Laundal & Richmond, 2017), and therefore easier to work with. This choice also avoids ambiguities related to secular variations in the magnetic field, and confusion about which type of magnetic coordinate systems is used. The apexpy Python module

(Emmert et al., 2010; van der Meeren et al., 2021) is used to find the magnetic eastward direction in Quasi-Dipole coordinates (Richmond, 1995), which we use to calculate $\mathbb{D}_{\hat{\mathbf{e}}_m}$ in Equation 50. Our code also has an option to make all calculations in centered dipole coordinates, which is convenient in some cases, like the examples shown in Section 4.1 which are based on synthetic data from simulations performed with a dipole magnetic field.

4. Results

In this section, we present a set of example applications of the Lompe technique. First, we demonstrate the technique with synthetic data based on an MHD simulation (Section 4.1). We also use the simulation output to give an example of how boundary effects influence the inversion. Then we present three examples with real data: In Section 4.2, we show an example using Iridium, SuperMAG, and SuperDARN data in a large grid that covers North America, with auroral conductance specified using a relatively simple empirical model. In Section 4.3, we show an example with conductance based on auroral imaging, but with no Iridium magnetometer data. In Section 4.4, we zoom in on a region with good coverage by SuperDARN. In all the examples with real data, we include measurements within a grid extended by 10 grid cells in each direction. Data further away would have very little influence due to the sharp decrease of the SECS functions (Equation 1).

4.1. Synthetic Test

Here, we present an example of applying the Lompe technique with synthetic simulated data, which means that we have perfect coverage and no uncertainty in the input, and we know what the output should be. To produce the synthetic data, we simulate the magnetospheric response to a solar wind pressure increase using the Grid Agnostic MHD for Extended Research Applications (GAMERA) code (Sorathia et al., 2020; Zhang et al., 2019). For our purposes, the specifics of the simulation are not very important, except that some structure in the ionospheric electrodynamics is preferred. The important point is that all the different quantities are consistently related. GAMERA ionospheric electric field and currents are calculated as described in Section 3.4, but with a different numerical scheme than used in the Lompe technique (Merkin & Lyon, 2010).

Figure 4 shows the GAMERA output in the first column, shown on a cubed-sphere projection. The top row shows electric potential (black contours), and Pedersen conductance in color. The Hall conductance is similar, but not shown. The next rows show, from top to bottom, the FAC, the eastward, northward, and upward components of the magnetic field disturbances on ground, and the eastward, northward, and upward components of the magnetic field disturbances at an altitude of 1,000 km, well above the horizontal current layer which is placed at 120 km. Except for the first column, all plots show Lompe output, when the input is the parameter indicated at the top. For example, the plot in the fifth column, second row, shows the Lompe FAC density when the northward magnetic field on ground is the only input to the inversion. Comparing this to the first column, which is the "ground truth" in this case, we see that it is faithfully reproduced.

In Figure 4, the regularization parameters are zero when the input is electric potential and FAC. That is, the solution is just a minimization of the least squares difference between input and model output. For the other columns, where the input is magnetic field components, we used $\lambda_1 = 0.1$ and $\lambda_2 = 0$ in Equation 50. With $\lambda_1 = 0$, all parameters except for the input were not well represented. The need for a tiny damping parameter shows that there are many electric fields which, given the conductance pattern, can produce the same pattern of magnetic field disturbances. That is, the inverse problem is ill-posed even with perfect data.

Figure 5 has the same format and the same simulated input data as in Figure 4, but a smaller analysis region. We have zoomed-in on a region that contains the spot with high conductance in the post-noon local time sector. We see that in general the retrieved patterns are similar to the original input data, but with some clear deviations. For example, the Lompe output FAC for magnetic field input has features at the boundary of the analysis region which are wrong. This result is expected: The magnetic field is a function of the global current system, not only the current within the analysis region; when we seek a current that is represented by SECS entirely within the analysis region, artificial edge structures emerge to account for remote currents. There is not much we can do about this except to be careful in the interpretation of the output patterns, unless we can add more information to constrain the electric field. The overall good fit in the interior region is encouraging, and shows that the Lompe output is useful if handled with some care. We discuss edge effects in more detail in Section 5.

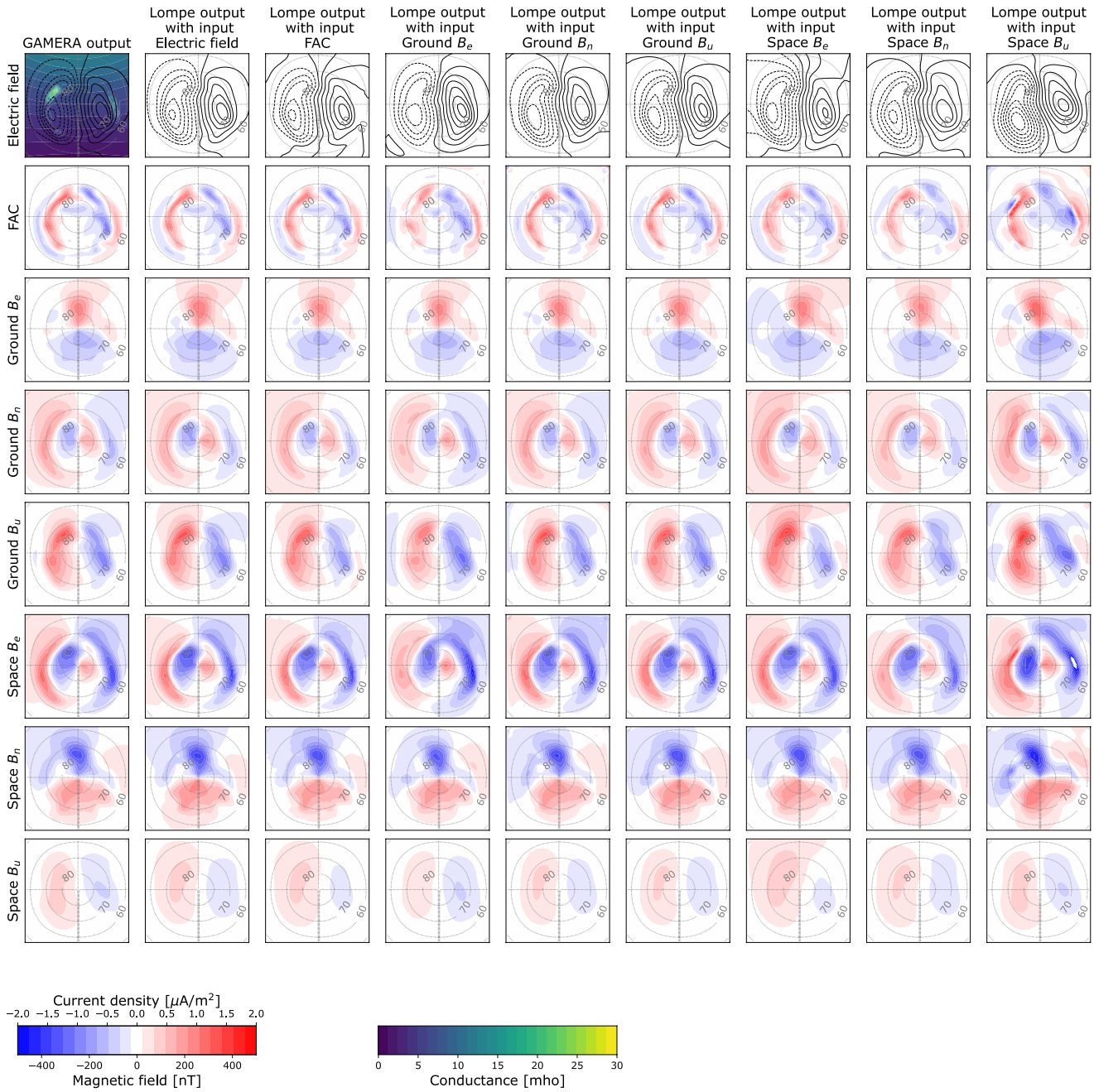

Figure 4. Results of Lompe inversions with synthetic data. The synthetic data comes from Grid Agnostic MHD for Extended Research Applications (GAMERA) magnetohydrodynamic (MHD) simulations, and the output is shown in the left column. Each row shows one quantity, indicated to the left. All plots, except for the left column, show Lompe inversion outputs. The eight rows correspond to eight different inputs to the inversion, indicated above the top row. The inversion result can be assessed by comparing the plots to the left column with GAMERA output, which can be considered to be the ground truth in this experiment. In this, and all following figures, upward field-aligned currents (FACs) are shown as red, and downward FACs blue.

In the rightmost columns of Figures 4 and 5, the input is the vertical magnetic field disturbances at 1,000-km altitude. In both figures, the Lompe output in this column is particularly poor compared to the other columns. Since the Lompe techniques assumes a vertical main field, the vertical magnetic field disturbances are not linked to FACs (Equation 9), but solely to divergence-free currents 880 km below (Equation 12). At this distance, small-scale structures in the ionospheric shell at 120 km contribute very little to the magnetic field. This is likely the reason for the notable deviations seen in the right columns. In the Lompe code (Laundal et al., 2022), there is an

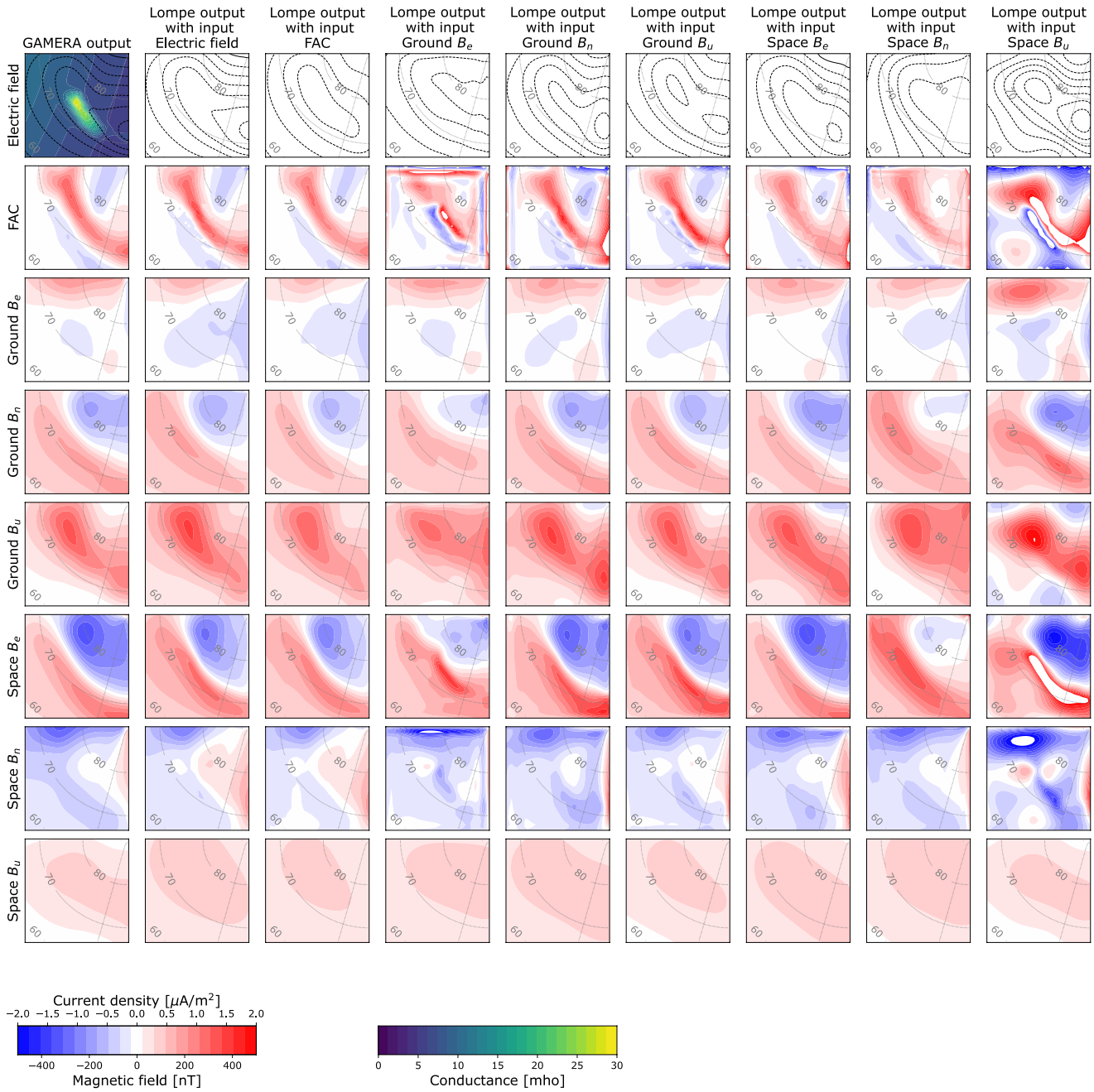

Figure 5. Results of Lompe inversions with synthetic data. The format and simulation data are the same as in Figure 4, except that this figure is based on input from, and shows output from, a much smaller region.

option to use space magnetometer data only to constrain FACs, intended for use with satellites at relatively high orbit and/or with relatively imprecise measurements.

4.2. North America Grid With Hardy Model Conductance

Figure 6 shows an example of the Lompe technique applied with real data. The analysis region covers much of North America and Greenland. Its extent is shown in black in Figure 1 in geographic coordinates, and in the top right panel of Figure 6 in magnetic apex coordinates (Richmond, 1995). The grid cell dimension is 100 × 100 km in the center and slightly larger toward the edges due to the cubed-sphere projection.

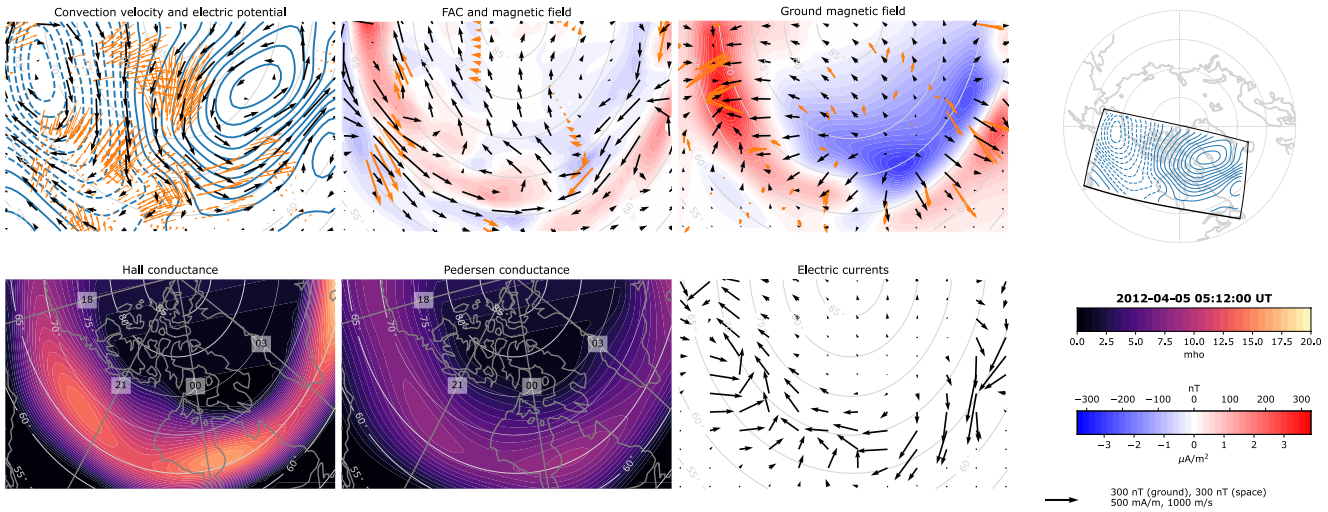

Figure 6. Lompe input and output for a 4-min time period centered at 5 April 2012 05:12 UT. The top row shows, from left to right: Convection flow field (SuperDARN line-of-sight measurements in orange) and electric potential contours; horizontal magnetic field disturbances 110 km above the ionosphere as black arrows and radial current density as color contours (Iridium horizontal magnetic field measurements in orange); horizontal ground magnetic field perturbations as black arrows and radial magnetic field perturbations as color contours (SuperMAG horizontal magnetic field perturbations as orange arrows); and a map that shows the grid's position and orientation with respect to apex magnetic latitude and local time. The bold grid edge corresponds to the lower edge of the projections shown in the other plots. The bottom row shows, from left to right: Pedersen conductance; Hall conductance; horizontal height-integrated ionospheric currents based on Lompe output; and color scale/vector scales.

The input data to the Lompe inversion in this example are SuperDARN line-of-sight convection measurements (Chisham et al., 2007), Iridium magnetometer measurements provided via AMPERE (Anderson et al., 2000; Waters et al., 2020), and ground magnetometer data provided via SuperMAG (Gjerloev, 2012). All data are from the 4 minutes starting at 05:12 UT on 5 April 2012. The input data are shown as orange vectors in the three top left panels, except for the vertical component of the ground magnetic field. The data are related to the electric field via the equations described in Sections 2 and 3 and the conductance maps shown in the bottom left panels. The conductances are a combination of auroral and EUV contributions; the EUV contribution is calculated as described in Section 2.4, and the auroral contribution is calculated with the relatively crude Hardy et al. (1987) empirical model with Kp = 4. The ionosphere is placed at 110-km altitude in this and the following examples.

The model parameters $\mathbf{m}$ were found from Equation 50 with $\lambda_1 = 1$ and $\lambda_2 = 10$. The corresponding convection pattern and electric potential are shown in the top left panel, together with the input data, all in a reference frame that rotates with the Earth. The black arrows in the next panel show the magnetic field in space, 110 km *above* the ionosphere, and the color contours show the vertical current density. The third panel from the left shows the ground magnetic field disturbances horizontal components as black vectors and vertical component as color contours. The panel below shows the horizontal height-integrated ionospheric currents.

We see that the inversion yields the night-side portion of a two-cell convection pattern with the dusk cell slightly wrapped around the dawn cell, so that plasma that leaves the polar cap on the dusk cell goes south-east and then west. This is the Harang reversal (Harang, 1946). Looking at the data (orange arrows), we see that the reversal in convection pattern has observational support. Beyond this qualitative statement, it is challenging to compare the input to the output in the convection map since the input is only in the line-of-sight direction. The FAC map is dominated by Region 1 and Region 2 currents as defined by Iijima and Potemra (1978), but some finer-scale structures are seen near the Harang reversal region. The radial magnetic field disturbance on ground is smooth and large-scale. The horizontal field exhibits sharp reversals in the left part of the map, which is seen in both the data and the inversion output.

To elucidate the effect of combining data sets in Figure 6, we show a contrasting example in Figure 7, where we have used the same setup as in Figure 6, but removed SuperDARN and Iridium data. The inversion in this figure is based only on ground magnetometer data, and is thus similar to the KRM technique (Kamide et al., 1981; Vanhamäki & Amm, 2007). We see that the dawn cell structure is largely similar, but the convection is stronger in the KRM version. The most striking difference between the figures is in the Harang reversal region, which

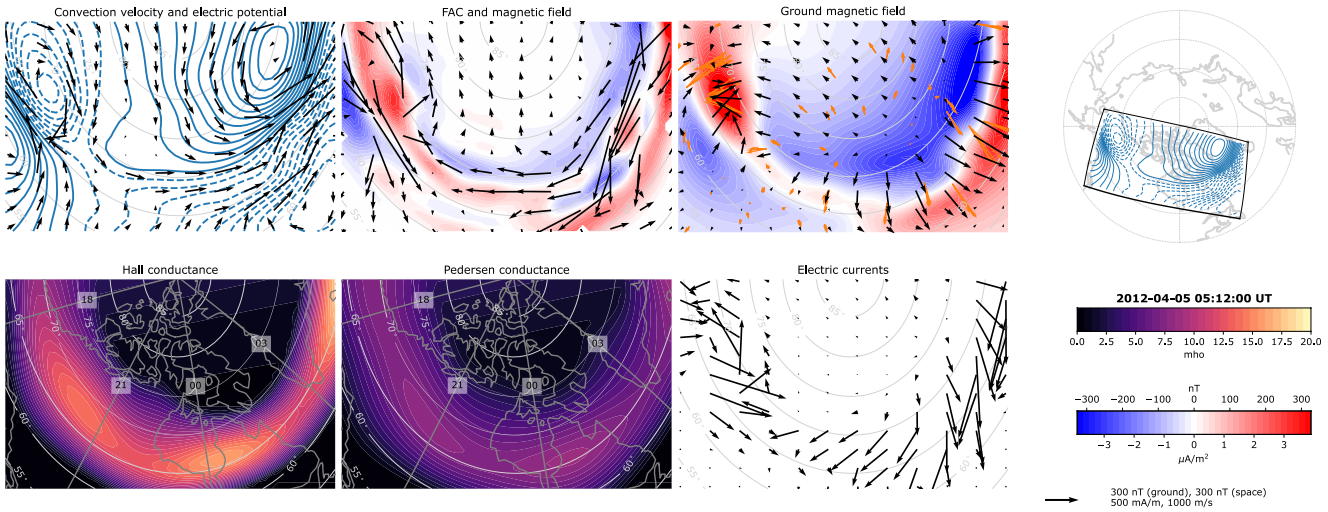

Figure 7. Same as Figure 6, except that we only use ground magnetometer data in the inversion.

is not well resolved with ground magnetometer data alone. We note again that the Hardy et al. (1987) auroral conductance model is crude, and that a better conductance estimate would improve the inversion results in both cases. Such estimates could come from more refined models (Newell et al., 2010; Zhang & Paxton, 2008) or from observations, as demonstrated below.

4.3. A High-Latitude Dayside Aurora Event

Figure 8 shows an example of the Lompe technique used with SuperMAG ground magnetic field data and SuperDARN line-of-sight convection measurements taken during a 4-min interval starting at 16:27 UT 17 August 2001. In this example, the auroral conductances were estimated based on a UV image of the aurora, taken by the Wideband Imaging Camera (WIC; Mende et al., 2000) on the Imager for Magnetopause-to-Aurora Global Exploration (IMAGE) satellite (Burch, 2000). The full auroral image is shown in Figure 9. We have removed contamination from sunlight using a model that is based on viewing geometry (Ohma et al., 2018). The corrected WIC intensity was converted to energy flux via relationships presented by Frey et al. (2003), assuming an average electron energy of 2.56 keV, and no contribution from protons. The estimated energy flux and assumed average energy were then used in the Robinson et al. (1987) formulae to obtain Hall and Pedersen conductances. Our

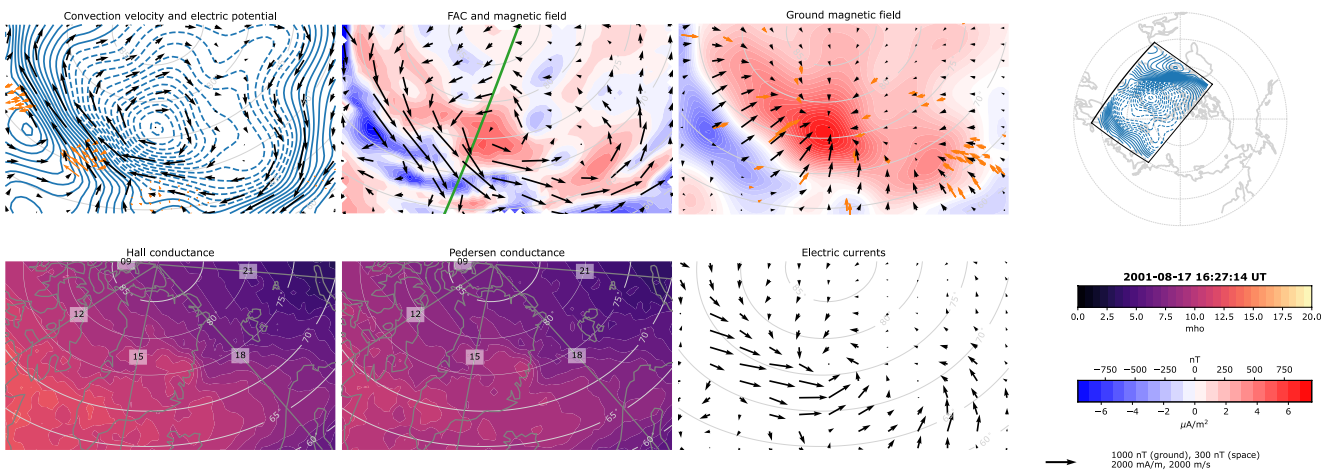

Figure 8. Lompe inversion results from 17 August 2001, using data from a 4-min interval starting at 16:27:14 UT. This was 2 min before a Wideband Imaging Camera (WIC) image was taken, which we use to estimate auroral conductance. The format of this figure is the same as for Figure 6. The green line in the field-aligned current (FAC) panel shows the satellite track of CHAMP, discussed further below, and in Figure 9.

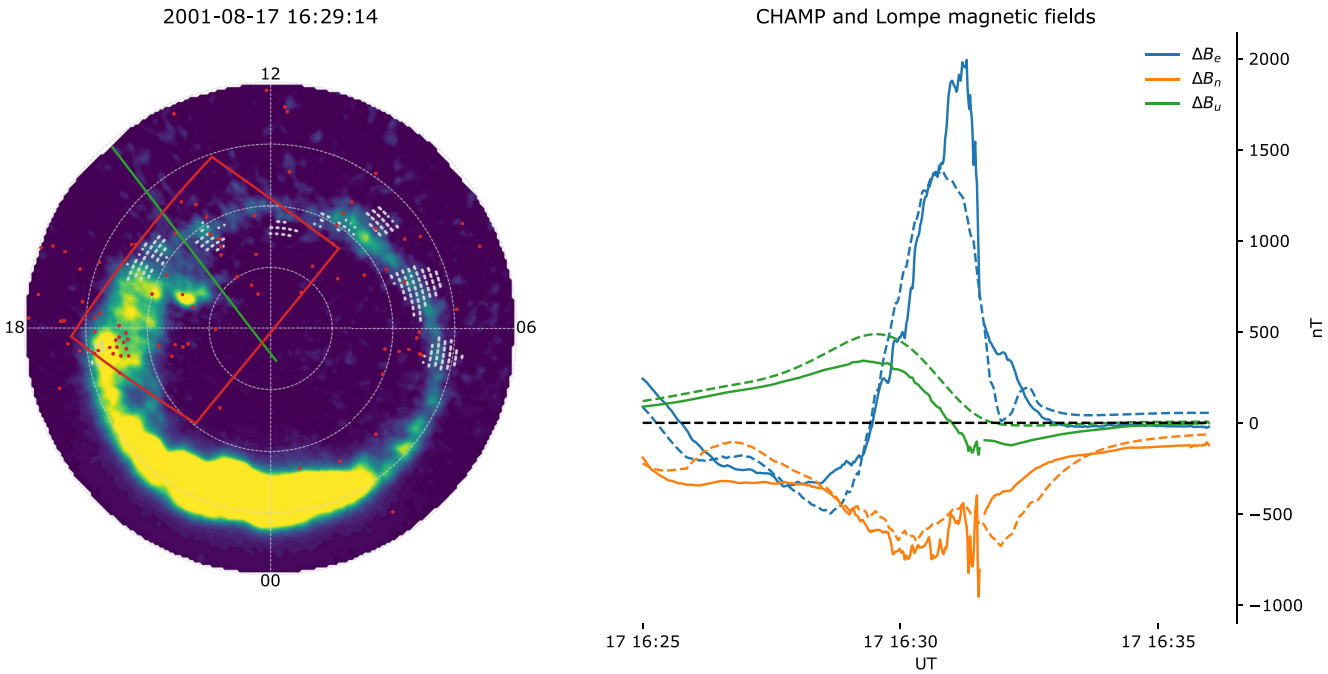

Figure 9. (left) The IMAGE WIC image used to estimate auroral conductance for the Lompe inversion discussed in Section 4.3 and displayed in Figure 8. The red dots show SuperMAG magnetometers, and gray dots show SuperDARN backscatter locations during the 4-min interval used in the inversion. The red frame shows the analysis region used in the Lompe inversion, and the green line shows the trajectory of the CHAMP satellite in a 10-min interval around the time of our analysis. (right) The magnetic field components measured by CHAMP (with the International Geomagnetic Reference Field (IGRF) main magnetic field subtracted), as solid lines. The dashed lines show the Lompe magnetic field evaluated at the same coordinates. The CHAMP data were not used as input in the Lompe inversion.

assumed average energy, which is close to that observed in particle measurements by a nearby DMSP satellite, gives a Hall-to-Pedersen ratio of 1. This method, despite large uncertainties, presumably yields much better representations of the auroral conductance and its gradients than the Hardy et al. (1987) model used in the example in Section 4.2. The solar EUV-induced conductance was added using the method described in Section 2.4. The result, displayed in Figure 8, show that the EUV conductance dominates. The Lompe inversion was done with data taken ±2 min relative to the time of the WIC image. In this inversion, $\lambda_1 = 1$ and $\lambda_2 = 10$ in Equation 50. The grid cells in the center are 75 × 75 km.

The Challenging Mini-satellite Payload (CHAMP) satellite passed over the analysis region at about 440-km altitude during the same time interval (green line in the FAC panel in Figure 8 and in the left panel of Figure 9). CHAMP carried a very accurate fluxgate magnetometer (Rother & Michaelis, 2019), and its 1 Hz measurements of the eastward, northward, and upward components of the magnetic field, with the main magnetic field (Alken et al., 2021) subtracted, are shown as solid lines in Figure 9 (right). The Lompe magnetic field, evaluated at the same positions as the CHAMP measurements, is shown as dashed lines. Although it would have been possible to include it (see Section 3.2.4), the CHAMP data were not used in the Lompe inversion. The good match demonstrates that the combination of ground magnetometer measurements, SuperDARN radar measurements, and reasonable conductance estimates, is sufficient to retrieve the magnetic field in space. Notice also that the steep decrease in the eastward magnetic field after it peaks matches well between CHAMP measurements and Lompe estimates. This is the very strong (≈7 μA/m^2) downward FAC which appears as a blue strip in Figure 8.

The data analyzed in this example is part of an event that was analyzed in detail by both Longley et al. (2016) and Østgaard et al. (2018). They conclude that the spot in the middle of the analysis region, which was present for several hours, is a so-called High-Latitude Dayside Aurora (HiLDA; Frey, 2007). Recently, Zhang et al. (2021) presented detailed images of what was presumably an HiLDA spot, and coined the term *space hurricane* since the spot had spiral arms like atmospheric hurricanes. The HiLDA spot/space hurricane is clearly visible in the WIC image displayed in Figure 9. It is a signature of lobe reconnection during times when the interplanetary magnetic field has a strong positive B_y component (or negative, if observed in the Southern hemisphere; Reistad et al., 2021).

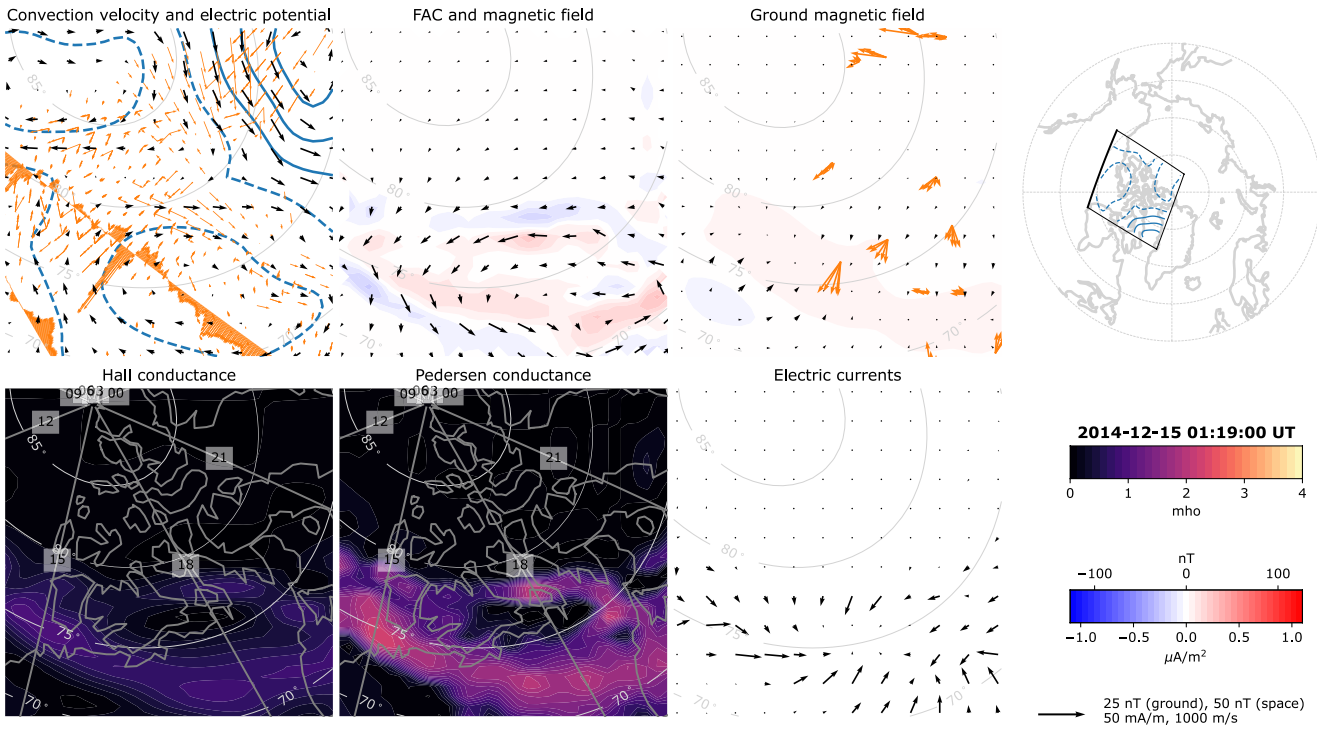

Figure 10. Event on 15 December 2014, at 01:19 UT during quiet conditions and northward IMF. Here, Lompe is used on a grid covering a region with good convection data coverage on the dusk side of the polar cap and auroral oval. The figure is on the same format as Figures 6–8. Conductance is estimated from simultaneous SSUSI LBHs emissions. Note the different magnitudes of the color scales and reference arrows compared to the previous test cases.

Østgaard et al. (2018) also sketched a convection pattern for this event based on a qualitative assessment of the available data and knowledge about statistical models. In agreement with our results, they suggested that ionospheric plasma circles clockwise around the auroral spot when viewed from above. Also, in agreement with our results, they suggested that the polar cap plasma enters the auroral oval at around 18–21 magnetic local time (MLT), signifying closure of magnetic flux via tail reconnection in this region (e.g., Laundal et al., 2010). However, Figure 8 also refines the pattern suggested by Østgaard et al. (2018), and reveals some unexpected features: On the night side of the spot, the convection is strongly reduced, and the polar cap plasma appears to go quite far toward dawn before turning back toward dusk, circling a large region of almost stagnant plasma. In addition to this, the Lompe results show much more channeled flows than suggested in the sketch by Østgaard et al. (2018): On the dayside, Lompe estimates reach flows of about 2,000 m/s, presumably driven by a combination of dayside and lobe reconnection. Return flows near 18 MLT reach almost the same level.

The Lompe inversion allows us to calculate the frictional heating rate from ions colliding with neutrals, often misleadingly referred to as Joule heating (Vasyliunas & Song, 2005). When the ionospheric Ohm's law is valid (see discussion of Equation 4) the heating rate is $W = \mathbf{E} \cdot \mathbf{J}$. Integrated over the analysis region, we find that it was >400 GW in this event. Most of this heating rate is concentrated in the convection channel just equatorward of the space hurricane. It is three times the maximum *global* heating rate reported by Weimer (2005) for average conditions with an IMF magnitude of 5 nT and solar wind velocity of 450 m/s. The Average Magnetic field and Polar current System (AMPS) model, presented by Laundal et al. (2018), shows that the strongest horizontal ionospheric currents occur near the dayside during conditions that are favorable for the space hurricane to occur. The AMPS model output and the strong heating rate reported here emphasize the importance of dayside dynamics in the total energy budget for magnetosphere-ionosphere coupling.

4.4. A Zoomed-In View With Convection Input During Quiet Conditions

Figure 10 shows the Lompe output on the same format as Figures 6–8 from an event on 15 December 2014, at 01:19 UT. The purpose of displaying this event is to further demonstrate the ability to resolve mesoscale

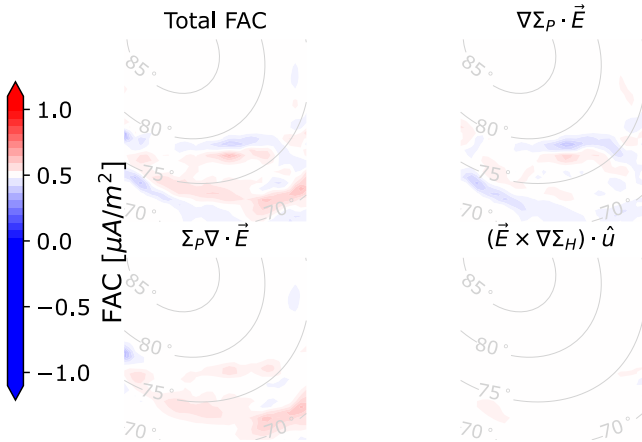

Figure 11. Separation of the three terms contributing to the field-aligned currents (FACs) in Equation 14. The upper left panel is the same as the FAC panel in Figure 10.

structures of the ionospheric electrodynamics in a limited spatial region when only line-of-sight convection measurements and precipitation characteristics are present, during typical quiet conditions. The grid used in Figure 10 has a resolution of 70 km in the horizontal directions and spans a region of about 2,500 km × 2,500 km. The conductance needed for the Lompe inversion is derived from the observed UV brightness of Lyman-Birge-Hopfield short (LBHs) wavelength (140–160 nm) emissions from the Special Sensor Ultraviolet Spectrographic Imager (SSUSI; Paxton et al., 1992) on-board the DMSP F18 satellite. As in the previous example using global FUV imaging, we assume a characteristic energy of the electron precipitation in the analysis region. Based on particle data from the in situ Special Sensor J (SSJ) instrument on DMSP F18, we find that a characteristic electron energy of 1 keV is representative. Further, using the estimated energy fluxes provided in the SSUSI Environmental Data Record Aurora files in regions of >500 R LBHs brightness within the grid, we find that a conversion factor of 472 R/(mW m^{-2}) can be used as a crude conversion from the LBHs irradiances to electron energy flux. From the estimated electron characteristic energy and energy flux, we use the empirical relationships presented by Robinson et al. (1987) to estimate Hall and Pedersen conductances. The median filtered binned averaged conductances based on SSUSI LBHs irradiances on the Lompe grid is seen in the two bottom panels in Figure 10. Note the difference in color scale compared to the previous examples. Furthermore, the EUV-induced solar conductance is very low throughout the entire analysis region.

SuperDARN gridded line-of-sight measurements from the interval 01:17–01:21 UT are used in the inversion. In addition, cross track ion drift measurements from the Special Sensor for Ions and Electrons and Scintillation (SSIES) instrument on simultaneous DMSP F17 and F18 passes are included, seen as orange stripes in the upper left panel in Figure 10. To obtain data across the entire analysis grid, DMSP data from the time interval 01:16–01:22 UT is used. This is the same time interval used to sample the LBHs emissions by SSUSI. We here use the same regularization parameters in the inversion as used in the above events, namely $\lambda_1 = 1$ and $\lambda_2 = 10$. On the western edge of the grid, we see convection toward the dayside inside the polar cap. The IMF Bz is positive (and small positive IMF By) at the time of the observations, after a northward turning at around 00:55 UT. We therefore suggest that the clockwise plasma circulation seen in the top left corner of the top left panel in Figure 10 is part of the dawn lobe cell. Sunward return flow within the oval at around 18 MLT is also seen, and anti-sunward convection poleward of the oval at the same local time.

The ionospheric currents and their associated perturbations in space and on ground, as estimated with the Lompe technique, are fairly weak due to the modest conductance values. Although not used in the inversion, ground magnetometer observations are illustrated in the third panel in the top row in Figure 10. It can be seen that the Lompe estimates of $\mathbf{\Delta B}$ on ground are much smaller than what is observed. This could be an effect of ground observatories being sensitive to disturbances from sources outside the analysis grid. This will be discussed in more detail in Section 5. It is also possible that our crude conductance estimates are too low. However, such an offset would largely affect the magnitude of the perturbations and not their spatial variation.

One advantage with the Lompe representation of the regional ionospheric electrodynamics is the ability to separate the different terms in Equation 14 contributing to the FACs. This decomposition is shown in Figure 11, showing how the three terms contribute to the total FAC. We can see that the main contributor is the term associated with the $\Sigma_P \nabla \cdot \mathbf{E}$ term, which is proportional with the Pedersen conductance and with the divergence of $\mathbf{E}$, or equivalently, using Equation 2, the flow vorticity. This is normally the dominating term in Equation 14 (e.g., Chisham et al., 2009; Reistad et al., 2019a). However, significant contributions especially to the downward currents (blue) is linked to Pedersen currents that flow across gradients in Σ_P. The third term, which describes the divergence of Hall currents as they flow across gradients in Σ_H is small in this case. This separation may be relevant to get further insights into the what controls the morphology of the ionospheric current system (Clayton et al., 2021). We emphasize that a realistic conductance must be provided to perform a reliable decomposition of the FACs.

5. Discussion

We have presented a new method for ionospheric data assimilation, combining different types of measurements via the ionospheric Ohm's law. The output of the method is a complete picture of ionospheric electrodynamics in an analysis region with flexible extent and spatial resolution. This technique for local mapping of polar ionospheric electrodynamics (Lompe) uses SECS as a basis. The short reach of these functions makes the Lompe technique potentially more suitable for regional analyses than existing techniques like AMIE. However, by choosing the analysis region large enough, as in the example shown in Figure 4, the Lompe technique can be seen as equivalent with AMIE, except with different basis functions. The Lompe technique can also be used in ways that can be considered as subclasses of the AMIE technique: By using only SuperDARN convection measurements and Iridium magnetometer data, the Lompe technique is equivalent with the analysis presented by Cousins et al. (2015). If we use only ground magnetometers as input, the Lompe technique is equivalent with the KRM technique (Kamide et al., 1981; Vanhamäki & Amm, 2007). If we use only ionospheric convection measurements as input, it is equivalent with the SECS analysis presented by Reistad et al. (2019), and almost equivalent with both the SECS analysis presented by Amm et al. (2010) and the Local Divergence-Free Fitting technique by Bristow et al. (2016).

We foresee that the main use case of the Lompe technique will be to produce maps of ionospheric electrodynamics in regions where the data density is high. We have shown two different examples from North America where we used grids with 100-km and 75-km resolution. It is likely that high data density in certain regions in North America and Fennoscandia could support analyses with even higher resolutions. Analyses in regions with high data density could resolve ionospheric dynamics at higher time resolutions than what is possible globally. This could help us understand the time-dependent ionospheric response to changes in the solar wind and the magnetosphere. For example, we know that substorms excite ionospheric convection (Grocott et al., 2009; Provan et al., 2004), but we do not know how fast it happens, or how the flow is organized with respect to the substorm bulge (e.g., Laundal et al., 2010). Understanding this coupling could also help us to understand how the ionospheric reaction may alter the imposed flows and influence magnetospheric dynamics (e.g., Elhawary et al., 2022; Lotko et al., 2014). Furthermore, as demonstrated in Section 4.3, the Lompe technique can be used to estimate frictional heating rates, which is an important driver of dynamics in the upper atmosphere (e.g., Ridley et al., 2006).

The Lompe technique could also be useful to increase the utility of certain measurements, such as multispectral imaging from GBOs (Clayton et al., 2019, 2021; Grubbs et al., 2018) and data from phased array incoherent scatter radars. For example, the EISCAT3D radar system (McCrea et al., 2015), which will be operational soon, will give ion flow measurements and ionospheric density in a volume above the field of view of the measurement sites. The ion flow measurements from the F-region can be used to derive the electric field, and the plasma density can be used to derive conductances. Combining this with data from surrounding magnetometer measurements with the Lompe technique can yield a more detailed view of the dynamics. Another example is the upcoming EZIE satellites, which will scan the magnetic field disturbances in the mesosphere as the satellites move. EZIE alone gives the equivalent divergence-free current (Laundal et al., 2021), and the Lompe technique can be used to combine EZIE data with other data sources to find the convection and FACs. Yet another use case could be for theoretical analyses and interpretations.

The Lompe technique uses a grid that is regular in a cubed-sphere projection (Ronchi et al., 1996). The grid can have arbitrary resolution, and arbitrary extent up to a point; our implementation currently only uses one face of a cube that circumscribes the Earth. However, we have limited freedom beyond this, unlike some earlier studies using SECS, where the nodes have been placed on an irregular grid (e.g., Weygand et al., 2011). This is not an option in our analysis, since the differentiation matrices $\mathbb{D}_{\mathbf{e}\cdot\nabla}$, $\mathbb{D}_{\mathbf{n}\cdot\nabla}$, and $\mathbb{D}_{\nabla\cdot}$ require regular grids.

The matrix equations presented in Section 3 essentially transform partial differential equations to algebraic equations (Vanhamäki & Juusola, 2020), which are solved by inversion. The partial differential equations are solved for $\mathbf{E}$ via the SECS amplitudes $\mathbf{m}$. Since we do not know how $\mathbf{E}$ varies on the boundary, we would not be able to find it via a boundary value problem. Instead, we use the data and a priori information to constrain the solution. We seek an electric field that fits the data, *and* which has a certain structure which we impose by regularization; the electric field should be relatively smooth, especially in the magnetic east-west direction. This information is not always sufficient to give meaningful results, however.

Figure 12 shows two examples to give some intuition for potential pitfalls when applying the Lompe technique. The left panel of Figure 12a shows an idealized input: An eastward flow field of 500 m/s everywhere except in a confined latitude band, indicated by dashed gray lines, where the flow field is 500 m/s in the westward direction. The conductance in the outer and inner regions is 10 and 0.01 mho, respectively. The current density and ground magnetic field implied by the Lompe inversion is shown to the right. The current density is as expected everywhere except at the boundary of the analysis domain where we see (relatively weak) FACs that are not consistent with uniform convection and conductance. These FACs reflect electric field SECS amplitudes that are needed to produce a uniform flow field in the inner region. It shows that one should be careful when interpreting the current densities near the boundaries of the analysis domain. The magnetic field perturbations shown in the panel below emphasize this point. They represent the magnetic field of *only* the currents that are in the analysis region. We would expect that, if the given flow field continued to be uniform in the east-west direction, the magnetic field perturbations only varied in the north-south direction. Instead, we see that the magnetic field changes toward the edges. This is because currents outside the domain are not accounted for.

Figure 12b illustrates how using the magnetic field as input can lead to wrong results. Here, our analysis region is confined to the rectangles in Figure 12a, where the conductance is low. Our input is the ground magnetic field in the output of Figure 12a. This magnetic field was mostly associated with currents in the high conductance surrounding region. Since we do not include that region in this analysis, the Lompe technique gives electric fields that are strong enough that currents inside the domain can explain the magnetic field perturbations. We see to the right that the current and flow field are completely wrong compared to the situation in Figure 12a. The flow field is 2 orders of magnitude too large. A realistic situation in which this could happen is if the analysis is confined to the dark polar cap, where the conductivity is extremely low due to the absence of sunlight and ionizing particle precipitation. Any nonzero magnetic field perturbation there must be associated with currents that are outside the analysis region. The Lompe technique would account for the magnetic field perturbations by amplifying the electric field to unrealistic levels. The problem can be reduced by increasing the size of the analysis region, and by using more data sources.

The latter example illustrates that the error can become quite large. The uncertainty in the Lompe estimates depends on the distribution of the data, measurement error, and on how the data are related to electric field amplitudes via the ionospheric Ohm's law. That means that the model error also depends on errors in the conductance, variations in the neutral wind (which we assume is zero), and the method by which unmodeled contributions to the measurements have been accounted for (e.g., contributions to the magnetic field from magnetospheric sources, the main magnetic field, or ground induction effects). In addition, regularization bias complicates the interpretation of model variance in terms of uncertainty (Aster et al., 2013). Quantifying the error is thus nontrivial, and something that we plan to return to in later development of the technique. It is likely that a Bayesian approach to the inversion would be fruitful in this respect, since it results in a distribution of solutions instead of one fixed vector $\mathbf{m}$.

A Bayesian approach could also help stabilize the solution in consecutive time steps. The later time step would be described by a probability distribution of model vectors, given any new data and a priori information which includes the model probability distribution from the previous time step. A dependence on the previous time step could also be implemented with the current inversion scheme by adding a term to the cost function f (Equation 49) that penalizes deviations from a prior model. Another potentially time-stabilizing addition, first suggested by Cousins et al. (2015), could be to link the conductance to the FAC of the previous time step; MHD simulations often use the Knight (1973) relation and Robinson et al. (1987) formulae to estimate how an upward current, carried by downward electrons, translates to auroral conductance. Another compelling solution is to coestimate the electric field amplitudes and conductances in one single inversion. This, however, is a nonlinear problem that requires a considerable change in how the inverse problem is solved.

The Lompe technique, as described in this paper, has been implemented in Python, and the code is available on Zenodo (Laundal et al., 2022). The inversion code includes tools for working with SECS and their magnetic fields, and a module for working with cubed-sphere grids (Ronchi et al., 1996). In addition the repository includes tools to treat SuperDARN, SuperMAG, and AMPERE's Iridium magnetometer data; visualization tools; a pure Python forward code for calculating International Geomagnetic Reference Field (IGRF) values; a Python implementation of the Hardy et al. (1987) auroral conductance model; functions that calculate the EUV produced conductance

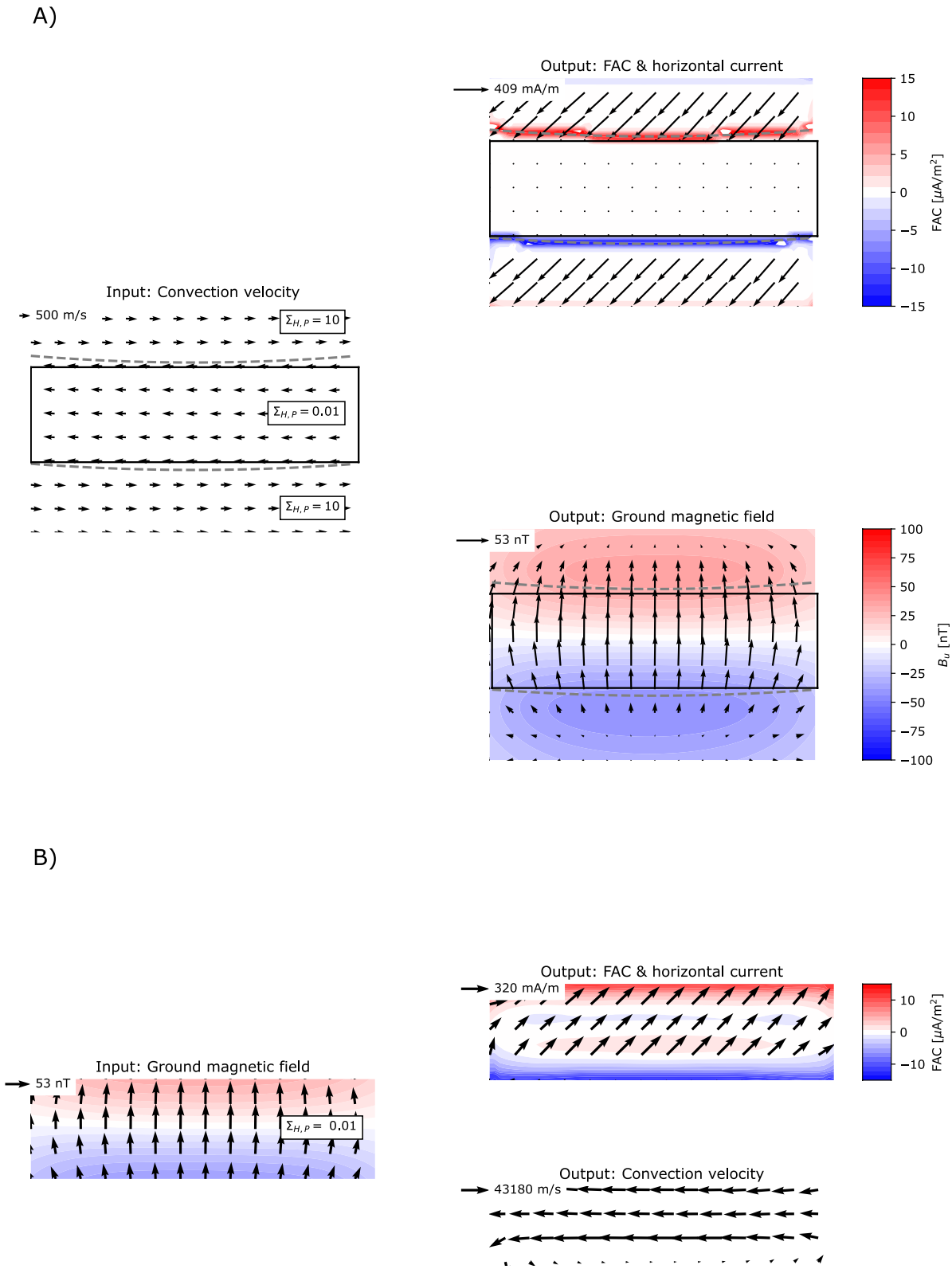

Figure 12. Two theoretical examples of how the Lompe inversion can give misleading results. (a) The input (left) is a flow field that is eastward except for in a confined latitude band (dashed gray lines) where it is westward. The conductance is 10 mho outside and 0.01 mho inside the band. The right plots show the current and ground magnetic field implied by Lompe inversion results. (b) The analysis region is the rectangle indicated in (a), and the input is the magnetic field from (a; shown to the left). The right plots show current densities and flow field implied by the Lompe inversion.

Acknowledgments
The University in Bergen group was supported by the Trond Mohn Foundation and by the Research Council of Norway under contracts 223252/F50 and 300844/F50. KAS acknowledges support from NASA Grants 80NSSC19K0241 and 80NSSC20K1833. V. G. Merkin and K. A. Sorathia acknowledge support from the NASA DRIVE Science Center for Geospace Storms (CGS), Grant 80NSSC20K0601. The development of the Lompe code was also helped by synergies with the AMPS model development, funded by ESA through the Swarm Data Innovation and Science Cluster (Swarm DISC) within the reference frame of ESA contract 000109587/13/I-NB. For more information on Swarm DISC, please visit https://earth.esa.int/eogateway/activities/swarm-disc. The authors would also like to thank the science team of the NASA EZIE mission for fruitful discussions. EZIE is the Heliophysics Science Mission which was selected to study electric currents in Earth's atmosphere linking aurora to the Earth's magnetosphere. EZIE will launch no earlier than September 2024. The principal investigator for the mission is Jeng-Hwa (Sam) Yee at the Johns Hopkins University Applied Physics Laboratory in Laurel, Maryland. We thank the International Space Science Institute in Bern, Switzerland, for hosting the team "Understanding Mesoscale Ionospheric Electrodynamics Using Regional Data Assimilation." We thank the team members for productive discussions about future developments. We are particularly grateful to Dr. Heikki Vanhamäki at the University of Oulu, Finland, for helpful comments and corrections. We thank the DMSP SSUSI team and P.I. Larry Paxton for use of SSUSI data. We thank Marc Hairston, the University of Texas at Dallas, for the DMSP SSIES data used in this study. For the ground magnetometer data, we gratefully acknowledge: INTERMAGNET, Alan Thomson; CARISMA, PI Ian Mann; CANMOS, Geomagnetism Unit of the Geological Survey of Canada; The S-RAMP Database, PI K. Yumoto and Dr. K. Shiokawa; The SPIDR database; AARI, PI Oleg Troshichev; The MACCS program, PI M. Engebretson; GIMA; MEASURE, UCLA IGPP and Florida Institute of Technology; SAMBA, PI Eftyhia Zesta; 210 Chain, PI K. Yumoto; SAMNET, PI Farideh Honary; IMAGE, PI Liisa Juusola; Finnish Meteorological Institute, PI Liisa Juusola; Sodankylä Geophysical Observatory, PI Tero Raita; UiT the Arctic University of Norway, Tromsø Geophysical Observatory, PI Magnar G. Johnsen; GFZ German Research Centre For Geosciences, PI Jürgen Matzka; Institute of Geophysics, Polish Academy of Sciences, PI Anne Neska and Jan Reda; Polar Geophysical Institute, PI Alexander Yahnin and Yarolav Sakharov; Geological Survey of Sweden, PI Gerhard Schwarz;

as described in Section 2.4; and Jupyter notebooks which serve as examples of how to use the code. All of the figures in this paper except Figure 2 are outputs from notebooks that can be found in the same code repository.

6. Conclusions

We have presented a new technique, called Lompe (Local mapping of polar ionospheric electrodynamics), to combine different types of measurements to yield a complete picture of ionospheric electrodynamics in a limited region. The technique combines magnetic field and convection measurements via the ionospheric Ohm's law. The technical implementation is based on SECS (Amm, 1997). Example applications presented in this paper show that the Lompe technique can be used to give a better understanding of the dynamics than what can be achieved with any individual data set alone. The Lompe technique is conceptually similar to the AMIE technique (Lu, 2017; Matsuo, 2020; Richmond & Kamide, 1988), but the use of SECS makes it arguably more flexible with respect to spatial extent and resolution.

A Python module that implements everything that is presented in this paper has been published (Laundal et al., 2022). This code also includes the novel method presented in Section 2.4 to calculate the EUV conductance, which does not lead to infinite gradients at the sunlight terminator. The technique and the code are being actively developed, and we plan to make improvements in error estimation, make the inversion more robust, and explore methods to stabilize the solution to give more reliable estimates of the spatiotemporal distribution of ionospheric electrodynamics.

Data Availability Statement

All data that have been used in this study are included in the Lompe code repository (Laundal et al., 2022) as sample data sets. This repository also contains code to reproduce all figures in the paper, except Figure 2. For using the Lompe technique in other events, we refer to the original data sources: The SSUSI EDR Aurora data product, which we use in Figure 10, can be downloaded from https://ssusi.jhuapl.edu/. DMSP SSIES data (used in Figure 10) are available at http://cedar.openmadrigal.org/. SuperMAG ground magnetometer data (used in Figures 1 and 6–10) are available from https://supermag.jhuapl.edu/. SuperDARN convection measurements (used in Figures 1, 6, and 8–11) were downloaded following the instructions at https://github.com/SuperDARNCanada/globus. See also the data set published by Thomas (2020). Iridium magnetometer data (used in Figures 1 and 6) were downloaded from http://ampere.jhuapl.edu/. WIC aurora images (used in Figures 8 and 9) can be accessed from https://spdf.gsfc.nasa.gov/pub/data/image/fuv/. CHAMP magnetic field measurements (Figure 9) are available through the Information System and Data Center, ISDC, at http://isdc.gfz-potsdam.de.

References

Alken, P., Thébault, E., Beggan, C. D., Amit, H., Aubert, J., Baerenzung, J., et al. (2021). International geomagnetic reference field: The thirteenth generation. *Earth, Planets and Space*, *73*(1), 49. https://doi.org/10.1186/s40623-020-01288-x

AMGeO Collaboration. (2019). A Collaborative Data Science Platform for the Geospace Community: Assimilative Mapping of Geospace Observations (AMGeO) v1.0.0 [Computer software manual]. (Supported by NSF ICER 1928403). https://doi.org/10.5281/zenodo.3564914

Amm, O. (1997). Ionospheric elementary current systems in spherical coordinates and their application. *Journal of Geomagnetism and Geoelectricity*, *49*, 947–955. https://doi.org/10.5636/jgg.49.947

Amm, O., Engebretson, M. J., Hughes, T., Newitt, L., Viljanen, A., & Watermann, J. (2002). A traveling convection vortex event study: Instantaneous ionospheric equivalent currents, estimation of field-aligned currents, and the role of induced currents. *Journal of Geophysical Research*, *107*(A11), 1334. https://doi.org/10.1029/2002JA009472

Amm, O., Grocott, A., Lester, M., & Yeoman, T. K. (2010). Local determination of ionospheric plasma convection from coherent scatter radar data using the SECS technique. *Journal of Geophysical Research*, *115*, A03304. https://doi.org/10.1029/2009JA014832

Amm, O., & Viljanen, A. (1999). Ionospheric disturbance magnetic field continuation from the ground to the ionosphere using spherical elementary current systems. *Earth Planets and Space*, *51*, 431–440. https://doi.org/10.1186/BF03352247

Anderson, B. J., Korth, H., Welling, D. T., Merkin, V. G., Wiltberger, M. J., Raeder, J., & Rastaetter, L. (2017). Comparison of predictive estimates of high-latitude electrodynamics with observations of global-scale Birkeland currents. *Space Weather*, *15*, 352–373. https://doi.org/10.1002/2016SW001529

Anderson, B. J., Takahashi, K., & Toth, B. A. (2000). Sensing global Birkeland currents with Iridium engineering magnetometer data. *Geophysical Research Letters*, *27*, 4045–4048. https://doi.org/10.1029/2000GL000094

Aster, R. C., Borchers, B., & Thurber, C. H. (2013). Chapter four—Tikhonov regularization. In R. C. Aster, B. Borchers, & C. H. Thurber (Eds.), *Parameter estimation and inverse problems* (2nd ed., pp. 93–127). Boston: Academic Press. https://doi.org/10.1016/B978-0-12-385048-5.00004-5

Birkeland, K. (1901). Résultats des rescherches magnéthiques faites par l'expédition Norvégienne de 1899–1900. *Archives des Sciences Physiques et Naturelles*, 565–586.

Swedish Institute of Space Physics, PI Masatoshi Yamauchi; AUTUMN, PI Martin Connors; DTU Space, Thom Edwards and PI Anna Willer; South Pole and McMurdo Magnetometer, PI's Louis J. Lanzarotti and Alan T. Weatherwax; ICESTAR; RAPIDMAG; British Artarctic Survey; McMac, PI Dr. Peter Chi; BGS, PI Dr. Susan Macmillan; Pushkov Institute of Terrestrial Magnetism, Ionosphere and Radio Wave Propagation (IZMIRAN); MFGI, PI B. Heilig; Institute of Geophysics, Polish Academy of Sciences, PI Anne Neska and Jan Reda; University of L'Aquila, PI M. Vellante; BCMT, V. Lesur and A. Chambodut; Data obtained in cooperation with Geoscience Australia, PI Andrew Lewis; AALPIP, co-PIs Bob Clauer and Michael Hartinger; MagStar, PI Jennifer Gannon; SuperMAG, PI Jesper W. Gjerloev; Data obtained in cooperation with the Australian Bureau of Meteorology, PI Richard Marshall. The authors acknowledge the use of SuperDARN data. SuperDARN is a collection of radars funded by national scientific funding agencies of Australia, Canada, China, France, Italy, Japan, Norway, South Africa, United Kingdom, and the United States of America.
We thank the AMPERE team and the AMPERE Science Center for providing the Iridium-derived data products. We thank S. B. Mende and the IMAGE FUV team at the Space Sciences Laboratory at UC Berkeley for the WIC image used in the 17 August 2001 event. The support of the CHAMP mission by the German Aerospace Center (DLR) and the Federal Ministry of Education and Research is gratefully acknowledged.

Bristow, W. A., Hampton, D. L., & Otto, A. (2016). High-spatial-resolution velocity measurements derived using local divergence-free fitting of SuperDARN observations. *Journal of Geophysical Research: Space Physics*, *121*, 1349–1361. https://doi.org/10.1002/2015JA021862

Burch, J. L. (2000). IMAGE mission overview. *Space Science Reviews*, *91*, 1–14. https://doi.org/10.1007/978-94-011-4233-5_1

Chartier, A. T., Huba, J. D., Sitaram, D. S., Merkin, V. G., Anderson, B. J., & Vines, S. K. (2022). High-latitude electrodynamics specified in Sami3 using ampere field-aligned currents. *Space Weather*, *20*, e2021SW002890. https://doi.org/10.1029/2021SW002890

Chisham, G., Freeman, M. P., Abel, G. A., Bristow, W. A., Marchaudon, A., Ruohoniemi, J. M., & Sofko, G. J. (2009). Spatial distribution of average vorticity in the high-latitude ionosphere and its variation with interplanetary magnetic field direction and season. *Journal of Geophysical Research*, *114*, A09301. https://doi.org/10.1029/2009JA014263

Chisham, G., Lester, M., Milan, S. E., Freeman, M. P., Bristow, W. A., Grocott, A., & Walker, A. D. M. (2007). A decade of the super dual auroral radar network (SuperDARN): Scientific achievements, new techniques and future directions. *Surveys in Geophysics*, *28*, 33–109. https://doi.org/10.1007/s10712-007-9017-8

Clayton, R., Burleigh, M., Lynch, K. A., Zettergren, M., Evans, T., Grubbs, G., & Varney, R. (2021). Examining the auroral ionosphere in three dimensions using reconstructed 2D maps of auroral data to drive the 3D GEMINI model. *Journal of Geophysical Research: Space Physics*, *126*, e2021JA029749. https://doi.org/10.1029/2021JA029749

Clayton, R., Lynch, K., Zettergren, M., Burleigh, M., Conde, M., Grubbs, G., & Varney, R. (2019). Two-dimensional maps of in situ ionospheric plasma flow data near auroral arcs using auroral imagery. *Journal of Geophysical Research: Space Physics*, *124*, 3036–3056. https://doi.org/10.1029/2018JA026440

Cousins, E. D. P., Matsuo, T., & Richmond, A. D. (2015). Mapping high-latitude ionospheric electrodynamics with SuperDARN and ampere. *Journal of Geophysical Research: Space Physics*, *120*, 5854–5870. https://doi.org/10.1002/2014JA020463

Dreher, J. (1997). On the self-consistent description of dynamic magnetosphere-ionosphere coupling phenomena with resolved ionosphere. *Journal of Geophysical Research*, *102*, 85–94. https://doi.org/10.1029/96JA02800

Edwards, T. R., Weimer, D. R., Olsen, N., Lühr, H., Tobiska, W. K., & Anderson, B. J. (2020). A third generation field-aligned current model. *Journal of Geophysical Research: Space Physics*, *125*, e2019JA027249. https://doi.org/10.1029/2019JA027249

Elhawary, R., Laundal, K. M., Reistad, J. P., & Hatch, S. M. (2022). Possible ionospheric influence on substorm onset location. *Geophysical Research Letters*, *49*, e2021GL096691. https://doi.org/10.1029/2021GL096691

Emmert, J. T., Richmond, A. D., & Drob, D. P. (2010). A computationally compact representation of Magnetic Apex and Quasi Dipole coordinates with smooth base vectors. *Journal of Geophysical Research*, *115*, A08322. https://doi.org/10.1029/2010JA015326

Förster, M., & Haaland, S. (2015). Interhemispheric differences in ionospheric convection: Cluster EDI observations revisited. *Journal of Geophysical Research: Space Physics*, *120*, 5805–5823. https://doi.org/10.1002/2014JA020774

Frey, H. U. (2007). Localized aurora beyond the auroral oval. *Reviews of Geophysics*, *45*, RG1003. https://doi.org/10.1029/2005RG000174

Frey, H. U., Mende, S. B., Immel, T. J., Gerard, J.-C., Hubert, B., Habraken, S., & Shemantovich, V. I. (2003). Summary of quantitative interpretation of IMAGE far ultraviolet auroral data. *Space Science Reviews*, *109*, 255–283. https://doi.org/10.1023/b:spac.0000007521.39348.a5

Fukushima, N. (1976). Generalized theorem for no ground magnetic effect of vertical currents connected with Pedersen currents in the uniform-conductivity ionosphere. *Report of Ionosphere and Space Research in Japan*, *30*, 35–50.

Gjerloev, J. W. (2012). The SuperMAG data processing technique. *Journal of Geophysical Research*, *117*, A09213. https://doi.org/10.1029/2012JA017683

Gjerloev, J. W., Waters, C. L., & Barnes, R. J. (2018). Deriving global convection maps from SuperDARN measurements. *Journal of Geophysical Research: Space Physics*, *123*, 2902–2915. https://doi.org/10.1002/2017JA024543

Grocott, A., Wild, J. A., Milan, S. E., & Yeoman, T. K. (2009). Superposed epoch analysis of the ionospheric convection evolution during substorms: Onset latitude dependence. *Annales Geophysicae*, *27*, 591–600. https://doi.org/10.5194/angeo-27-591-2009

Grubbs, G., Michell, R., Samara, M., Hampton, D., & Jahn, J.-M. (2018). Predicting electron population characteristics in 2-D using multispectral ground-based imaging. *Geophysical Research Letters*, *45*, 15–20. https://doi.org/10.1002/2017GL075873

Haines, G. V. (1985). Spherical cap harmonic analysis. *Journal of Geophysical Research*, *90*, 2583–2591. https://doi.org/10.1029/JB090iB03p02583

Harang, L. (1946). The mean field of disturbance of polar geomagnetic storms. *Terrestrial Magnetism and Atmospheric Electricity*, *51*(3), 353–380. https://doi.org/10.1029/TE051i003p00353

Hardy, D. A., Gussenhoven, M. S., Raistrick, R., & McNeil, W. J. (1987). Statistical and functional representation of the pattern of auroral energy flux, number flux, and conductivity. *Journal of Geophysical Research*, *92*, 12275–12294. https://doi.org/10.1029/JA092iA11p12275

Heppner, J. P., & Maynard, N. C. (1987). Empirical high-latitude electric field models. *Journal of Geophysical Research*, *92*, 4467–4489. https://doi.org/10.1029/JA092iA05p04467

Huestis, D. L. (2001). Accurate evaluation of the chapman function for atmospheric attenuation. *Journal of Quantitative Spectroscopy and Radiative Transfer*, *69*(6), 709–721. https://doi.org/10.1016/S0022-4073(00)00107-2

Ieda, A., Oyama, S., Vanhamäki, H., Fujii, R., Nakamizo, A., Amm, O., & Nishitani, N. (2014). Approximate forms of daytime ionospheric conductance. *Journal of Geophysical Research: Space Physics*, *119*, 10397–10415. https://doi.org/10.1002/2014JA020665

Iijima, T., & Potemra, T. A. (1978). Large-scale characteristics of field-aligned currents associated with substorms. *Journal of Geophysical Research*, *83*, 599–615. https://doi.org/10.1029/JA083iA02p00599

Juusola, L., Milan, S. E., Lester, M., Grocott, A., & Imber, S. M. (2014). Interplanetary magnetic field control of the ionospheric field-aligned current and convection distributions. *Journal of Geophysical Research: Space Physics*, *119*, 3130–3149. https://doi.org/10.1002/2013JA019455

Kamide, Y., Richmond, A. D., & Matsushita, S. (1981). Estimation of ionospheric electric fields, ionospheric currents, and field-aligned currents from ground magnetic records. *Journal of Geophysical Research*, *86*, 801–813. https://doi.org/10.1029/JA086iA02p00801

Knight, S. (1973). Parallel electric fields. *Planetary and Space Science*, *21*, 741. https://doi.org/10.1016/0032-0633(73)90093-7

Knudsen, D. J., Burchill, J. K., Buchert, S. C., Eriksson, A. I., Gill, R., Wahlund, J.-E., & Moffat, B. (2017). Thermal ion imagers and Langmuir probes in the swarm electric field instruments. *Journal of Geophysical Research: Space Physics*, *122*, 2655–2673. https://doi.org/10.1002/2016JA022571

Laundal, K. M., Finlay, C. C., & Olsen, N. (2016). Sunlight effects on the 3D polar current system determined from low Earth orbit measurements. *Earth, Planets and Space*, *68*, 142. https://doi.org/10.1186/s40623-016-0518-x

Laundal, K. M., Finlay, C. C., Olsen, N., & Reistad, J. P. (2018). Solar wind and seasonal influence on ionospheric currents from Swarm and CHAMP measurements. *Journal of Geophysical Research: Space Physics*, *123*, 4402–4429. https://doi.org/10.1029/2018JA025387

Laundal, K. M., Haaland, S. E., Lehtinen, N., Gjerloev, J. W., Ostgaard, N., Tenfjord, P., & Anderson, B. J. (2015). Birkeland current effects on high-latitude ground magnetic field perturbations. *Geophysical Research Letters*, *42*, 7248–7254. https://doi.org/10.1002/2015GL065776

Laundal, K. M., Hovland, A. O., Hatch, S. M., Reistad, J. P., Walker, S. J., & Madelaire, M. (2022). Local mapping of polar ionospheric electrodynamics (Lompe). *Zenodo*. https://doi.org/10.5281/zenodo.5973850

Laundal, K. M., Østgaard, N., Frey, H. U., & Weygand, J. M. (2010). Seasonal and interplanetary magnetic field-dependent polar cap contraction during substorm expansion phase. *Journal of Geophysical Research*, *115*, A11224. https://doi.org/10.1029/2010JA015910

Laundal, K. M., Østgaard, N., Snekvik, K., & Frey, H. U. (2010). Inter-hemispheric observations of emerging polar cap asymmetries. *Journal of Geophysical Research*, *115*, A07230. https://doi.org/10.1029/2009JA015160

Laundal, K. M., & Richmond, A. D. (2017). Magnetic coordinate systems. *Space Science Reviews*, *206*, 27–59. https://doi.org/10.1007/s11214-016-0275-y

Laundal, K. M., Yee, J. H., Merkin, V. G., Gjerloev, J. W., Vanhamäki, H., Reistad, J. P., & Espy, P. J. (2021). Electrojet estimates from mesospheric magnetic field measurements. *Journal of Geophysical Research: Space Physics*, *126*, e2020JA028644. https://doi.org/10.1029/2020JA028644

Longley, W., Reiff, P., Reistad, J. P., & Østgaard, N. (2016). Magnetospheric model performance during conjugate aurora. In *Magnetosphere-ionosphere coupling in the solar system* (pp. 227–233). American Geophysical Union (AGU). https://doi.org/10.1002/9781119066880.ch18

Lotko, W., Smith, R. H., Zhang, B., Ouellette, J. E., Brambles, O. J., & Lyon, J. G. (2014). Ionospheric control of magnetotail reconnection. *Science*, *345*, 184–187. https://doi.org/10.1126/science.1252907

Lu, G. (2017). Large scale high-latitude ionospheric electrodynamic fields and currents. *Space Science Reviews*, *206*, 431–450. https://doi.org/10.1007/s11214-016-0269-9

Matsuo, T. (2020). *Recent progress on inverse and data assimilation procedure for high-latitude ionospheric electrodynamics*. https://doi.org/10.1007/978-3-030-26732-2_10

McCrea, I., Aikio, A., Alfonsi, L., Belova, E., Buchert, S., Clilverd, M., et al. (2015). The science case for the EISCAT_3D radar. *Progress in Earth and Planetary Science*, *2*(1), 21. https://doi.org/10.1186/s40645-015-0051-8

Mende, S. B., Harris, S. E., Frey, H. U., Angelopoulos, V., Russell, C. T., Donovan, E., & Peticolas, L. M. (2008). The THEMIS array of ground-based observatories for the study of auroral substorms. *Space Science Reviews*, *141*(1), 357. https://doi.org/10.1007/s11214-008-9380-x

Mende, S. B., Heetderks, H., Frey, H. U., Lampton, M., Geller, S. P., Abiad, R., & Trondsen, T. (2000). Far ultraviolet imaging from the IMAGE spacecraft. 2. Wideband FUV imaging. *Space Science Reviews*, *91*, 271–285. https://doi.org/10.1007/978-94-011-4233-5_9

Merkin, V. G., & Lyon, J. G. (2010). Effects of the low-latitude ionospheric boundary condition on the global magnetosphere. *Journal of Geophysical Research*, *115*, A10202. https://doi.org/10.1029/2010JA015461

Moen, J., & Brekke, A. (1993). The solar flux influence on quiet time conductances in the auroral ionosphere. *Geophysical Research Letters*, *20*, 971–974. https://doi.org/10.1029/92GL02109

Nakano, S., Hori, T., Seki, K., & Nishitani, N. (2020). A framework for estimating spherical vector fields using localized basis functions and its application to SuperDARN data processing. *Earth, Planets and Space*, *72*, 46. https://doi.org/10.1186/s40623-020-01168-4

Newell, P. T., Sotirelis, T., & Wing, S. (2010). Seasonal variations in diffuse, monoenergetic, and broadband aurora. *Journal of Geophysical Research*, *115*, A03216. https://doi.org/10.1029/2009JA014805

Nicolls, M. J., Cosgrove, R., & Bahcivan, H. (2014). Estimating the vector electric field using monostatic, multibeam incoherent scatter radar measurements. *Radio Science*, *49*, 1124–1139. https://doi.org/10.1002/2014RS005519

Ohma, A., Østgaard, N., Reistad, J. P., Tenfjord, P., Laundal, K. M., Snekvik, K., & Fillingim, M. O. (2018). Evolution of asymmetrically displaced footpoints during substorms. *Journal of Geophysical Research: Space Physics*, *123*, 10030–10063. https://doi.org/10.1029/2018JA025869

Østgaard, N., Reistad, J. P., Tenfjord, P., Laundal, K. M., Rexer, T., Haaland, S. E., & Ohma, A. (2018). The asymmetric geospace as displayed during the geomagnetic storm on 17 August 2001. *Annales Geophysicae*, *36*(6), 1577–1596. https://doi.org/10.5194/angeo-36-1577-2018

Paxton, L. J., Meng, C.-I., Fountain, G. H., Ogorzalek, B. S., Darlington, E. H., Gary, S. A., et al. (1992). *Special sensor ultraviolet spectrographic imager: An instrument description* (Vol. 1745, pp. 2–15). Proceedings of SPIE. https://doi.org/10.1117/12.60595

Pettigrew, E. D., Shepherd, S. G., & Ruohoniemi, J. M. (2010). Climatological patterns of high-latitude convection in the Northern and Southern hemispheres: Dipole tilt dependencies and interhemispheric comparison. *Journal of Geophysical Research*, *115*, A07305. https://doi.org/10.1029/2009JA014956

Provan, G., Lester, M., Mende, S. B., & Milan, S. E. (2004). Statistical study of high-latitude plasma flow during magnetospheric substorms. *Annals of Geophysics*, *22*, 3607–3624. https://doi.org/10.5194/angeo-22-3607-2004

Reistad, J. P., Laundal, K. M., Østgaard, N., Ohma, A., Burrell, A. G., Hatch, S. M., & Thomas, E. G. (2021). Quantifying the lobe reconnection rate during dominant IMF by periods and different dipole tilt orientations. *Journal of Geophysical Research: Space Physics*, *126*, e2021JA029742. https://doi.org/10.1029/2021JA029742

Reistad, J. P., Laundal, K. M., Østgaard, N., Ohma, A., Haaland, S., Oksavik, K., & Milan, S. E. (2019). Separation and quantification of ionospheric convection sources: 1. A new technique. *Journal of Geophysical Research: Space Physics*, *124*, 6343–6357. https://doi.org/10.1029/2019JA026634

Reistad, J. P., Laundal, K. M., Østgaard, N., Ohma, A., Thomas, E. G., Haaland, S., & Milan, S. E. (2019). Separation and quantification of ionospheric convection sources: 2. The dipole tilt angle influence on reverse convection cells during northward IMF. *Journal of Geophysical Research: Space Physics*, *124*, 6182–6194. https://doi.org/10.1029/2019JA026641

Rich, F. J. (1994). *Users Guide for the Topside Ionospheric Plasma Monitor (SSIES, SSIES-2 and SSIES-3) on Spacecraft of the Defense Meteorological Satellite Program* (Vol. 1). Technical description.

Richmond, A. D. (1995). Ionospheric electrodynamics using magnetic apex coordinates. *Journal of Geomagnetism and Geoelectricity*, *47*, 191–212. https://doi.org/10.5636/jgg.47.191

Richmond, A. D., & Kamide, Y. (1988). Mapping electrodynamic features of the high-latitude ionosphere from localized observations: Technique. *Journal of Geophysical Research*, *93*, 5741–5759. https://doi.org/10.1029/JA093iA06p05741

Ridley, A., Deng, Y., & Tóth, G. (2006). The global ionosphere-thermosphere model. *Journal of Atmospheric and Solar-Terrestrial Physics*, *68*(8), 839–864. https://doi.org/10.1016/j.jastp.2006.01.008

Robinson, R. M., Vondrak, R. R., Miller, K., Dabbs, T., & Hardy, D. (1987). On calculating ionospheric conductances from the flux and energy of precipitating electrons. *Journal of Geophysical Research*, *92*, 2565–2569. https://doi.org/10.1029/JA092iA03p02565

Robinson, R. M., Zanetti, L., Anderson, B., Vines, S., & Gjerloev, J. (2021). Determination of auroral electrodynamic parameters from ampere field-aligned current measurements. *Space Weather*, *19*, e2020SW002677. https://doi.org/10.1029/2020SW002677

Ronchi, C., Iacono, R., & Paolucci, P. S. (1996). The "cubed sphere": A new method for the solution of partial differential equations in spherical geometry. *Journal of Computational Physics*, *124*(1), 93–114. https://doi.org/10.1006/jcph.1996.0047

Rother, M., & Michaelis, I. (2019). *CH-ME-3-MAG-CHAMP 1 Hz combined magnetic field time series (level 3)*. GFZ Data Services. https://doi.org/10.5880/GFZ.2.3.2019.004

Ruohoniemi, J. M., & Baker, K. B. (1998). Large-scale imaging of high-latitude convection with super dual auroral radar network HF radar observations. *Journal of Geophysical Research*, *103*, 20797–20811. https://doi.org/10.1029/98JA01288

Schunk, R., & Nagy, A. (2009). *Ionospheres: Physics, plasma physics, and chemistry* (2nd ed.). Cambridge University Press. https://doi.org/10.1017/CBO9780511635342

Sorathia, K. A., Merkin, V. G., Panov, E. V., Zhang, B., Lyon, J. G., Garretson, J., & Wiltberger, M. (2020). Ballooning-interchange instability in the near-Earth plasma sheet and auroral beads: Global magnetospheric modeling at the limit of the MHD approximation. *Geophysical Research Letters*, *47*, e2020GL088227. https://doi.org/10.1029/2020GL088227

Thomas, E. G. (2020). SuperDARN grid files used to create the Thomas and Shepherd [2018] statistical convection model. *Zenodo*. https://doi.org/10.5281/zenodo.3618607

Untiedt, J., & Baumjohann, W. (1993). Studies of polar current systems using the IMS Scandinavian magnetometer array. *Space Science Reviews*, *63*, 245–390. https://doi.org/10.1007/BF00750770

van der Meeren, C., Laundal, K. M., Burrell, A. G., Starr, G., Reimer, A. S., & Morschhauser, A. (2021). aburrell/apexpy: Apexpy version 1.1.0. *Zenodo*, (When referencing this package, please cite both the package DOI and the Apex Coordinates journal article: Emmert, J. T., Richmond, A. D., & Drob, D. P. (2010), A computationally compact representation of Magnetic-Apex and Quasi-Dipole coordinates with smooth base vectors, Journal of Geophysical ResearchJ. Geophys. Res., 115(A8), A08322, 10.1029/2010JA015326) https://doi.org/10.5281/zenodo.4585641

Vanhamäki, H., & Amm, O. (2007). A new method to estimate ionospheric electric fields and currents using data from a local ground magnetometer network. *Annales Geophysicae*, *25*(5), 1141–1156. https://doi.org/10.5194/angeo-25-1141-2007

Vanhamäki, H., & Juusola, L. (2020). Introduction to spherical elementary current systems. In *Ionospheric multi-spacecraft analysis tools* (Vol. 17, pp. 5–33). ISSI Scientific Report Series. https://doi.org/10.1007/978-3-030-26732-2_2

Vasyliunas, V. M., & Song, P. (2005). Meaning of ionospheric Joule heating. *Journal of Geophysical Research*, *110*, A02301. https://doi.org/10.1029/2004JA010615

Vestine, E. H., Laporte, L., Lange, I., & Scott, W. E. (1947). *The geomagnetic field, its description and analysis*. Carnegie Institution of Washington.

Waters, C. L., Anderson, B. J., Green, D. L., Korth, H., Barnes, R. J., & Vanhamäki, H. H. (2020). Science data products for ampere. In M. W.Dunlop, & H.Lühr (Eds.), *Ionospheric multi-spacecraft analysis tools: Approaches for deriving ionospheric parameters* (pp. 141–165). Cham: Springer International Publishing. https://doi.org/10.1007/978-3-030-26732-2_7

Waters, C. L., Gjerloev, J. W., Dupont, M., & Barnes, R. J. (2015). Global maps of ground magnetometer data. *Journal of Geophysical Research: Space Physics*, *120*, 9651–9660. https://doi.org/10.1002/2015JA021596

Weimer, D. R. (2005). Improved ionospheric electrodynamic models and application to calculating joule heating rates. *Journal of Geophysical Research*, *110*, A05306. https://doi.org/10.1029/2004JA010884

Weimer, D. R. (2013). An empirical model of ground-level geomagnetic perturbations. *Space Weather*, *11*, 107–120. https://doi.org/10.1002/swe.20030

Weygand, J. M., Amm, O., Viljanen, A., Angelopoulos, V., Murr, D., Engebretson, M. J., & Mann, I. (2011). Application and validation of the spherical elementary currents systems technique for deriving ionospheric equivalent currents with the north American and Greenland ground magnetometer arrays. *Journal of Geophysical Research*, *116*, A03305. https://doi.org/10.1029/2010JA016177

Wiltberger, M., Wang, W., Burns, A. G., Solomon, S. C., Lyon, J. G., & Goodrich, C. C. (2004). Initial results from the coupled magnetosphere ionosphere thermosphere model: Magnetospheric and ionospheric responses. *Journal of Atmospheric and Solar-Terrestrial Physics*, *66*, 1411–1423. https://doi.org/10.1016/j.jastp.2004.03.026

Yee, J. H., Gjerloev, J., Wu, D., & Schwartz, M. J. (2017). First application of the zeeman technique to remotely measure auroral electrojet intensity from space. *Geophysical Research Letters*, *44*, 10134–10139. https://doi.org/10.1002/2017GL074909

Zhang, B., Sorathia, K. A., Lyon, J. G., Merkin, V. G., Garretson, J. S., & Wiltberger, M. (2019). Gamera: A three-dimensional finite-volume MHD solver for non-orthogonal curvilinear geometries. *The Astrophysical Journal-Supplement Series*, *244*(1), 20. https://doi.org/10.3847/1538-4365/ab3a4c

Zhang, Q.-H., Zhang, Y.-L., Wang, C., Oksavik, K., Lyons, L. R., Lockwood, M., & Xia, L.-D. (2021). A space hurricane over the Earth's polar ionosphere. *Nature Communications*, *12*(1), 1207. https://doi.org/10.1038/s41467-021-21459-y

Zhang, Y., & Paxton, L. (2008). An empirical kp-dependent global auroral model based on timed/guvi fuv data. *Journal of Atmospheric and Solar-Terrestrial Physics*, *70*(8), 1231–1242. https://doi.org/10.1016/j.jastp.2008.03.008